

## The ALMA-ATOMS-QUARKS survey: Resolving a chemically rich massive protostellar outflow

JIA-HANG ZOU  <sup>1,2</sup> TIE LIU  <sup>2</sup> FENGWEI XU  <sup>3,4</sup> XINDI TANG  <sup>5</sup> DEZHAO MENG  <sup>5,6,2</sup> YAN-KUN ZHANG  <sup>2</sup>,  
 AIYUAN YANG  <sup>7,8</sup> TAPAS BAUG, <sup>9</sup> CHANG-WON LEE  <sup>10,11</sup> L. VIKTOR TÓTH  <sup>12,13</sup> ARIFUL HOQUE  <sup>9</sup> SAMI DIB  <sup>14</sup>,  
 PABLO GARCIA  <sup>15,16</sup> HONG-LI LIU  <sup>1</sup> PRASANTA GORAI, <sup>17,18</sup> SWAGAT R. DAS  <sup>19</sup> GUIDO GARAY, <sup>15,19</sup>  
 PATRICIO SANHUEZA  <sup>20</sup> LI CHEN  <sup>1</sup>, DI LI, <sup>21</sup> JIHYE HWANG  <sup>22,23</sup> AND DONGTING YANG

THE ATOMS-QUARKS COLLABORATION

<sup>1</sup> School of Physics and Astronomy, Yunnan University, Kunming 650091, People's Republic of China

<sup>2</sup> Shanghai Astronomical Observatory, Chinese Academy of Sciences, 80 Nandan Road, Shanghai 200030, People's Republic of China

<sup>3</sup> Max Planck Institute for Astronomy, Königstuhl 17, 69117 Heidelberg, Germany

<sup>4</sup> Kavli Institute for Astronomy and Astrophysics, Peking University, 5 Yiheyuan Road, Haidian District, Beijing 100871, People's Republic of China

<sup>5</sup> Xinjiang Astronomical Observatory, Chinese Academy of Sciences, 830011 Urumqi, People's Republic of China

<sup>6</sup> University of Chinese Academy of Sciences, Beijing 100080, People's Republic of China

<sup>7</sup> National Astronomical Observatories, Chinese Academy of Sciences, Beijing 100101, People's Republic of China

<sup>8</sup> Key Laboratory of Radio Astronomy and Technology, Chinese Academy of Sciences, A20 Datun Road, Chaoyang District, Beijing, 100101, People's Republic of China

<sup>9</sup> S. N. Bose National Centre for Basic Sciences, Block-JD, Sector-III, Salt Lake City, Kolkata 700106, India

<sup>10</sup> University of Science and Technology, Korea (UST), 217 Gajeong-ro, Yuseong-gu, Daejeon 34113, Republic of Korea

<sup>11</sup> Korea Astronomy and Space Science Institute, 776 Daedeokdaero, Yuseong-gu, Daejeon 34055, Republic of Korea

<sup>12</sup> Institute of Physics and Astronomy, Eötvös Loránd University, Pázmány Péter sétány 1/A, H-1117 Budapest, Hungary

<sup>13</sup> Faculty of Science and Technology, University of Debrecen, H-4032 Debrecen, Hungary

<sup>14</sup> Max Planck Institute for Astronomy, Königstuhl 17, 69117, Heidelberg, Germany

<sup>15</sup> Chinese Academy of Sciences South America Center for Astronomy, National Astronomical Observatories, CAS, Beijing 100101, China

<sup>16</sup> Instituto de Astronomía, Universidad Católica del Norte, Av. Angamos 0610, Antofagasta, Chile

<sup>17</sup> Nansen Centre for Solar Physics, University of Oslo, PO Box 1029 Blindern, 0315 Oslo, Norway

<sup>18</sup> Institute of Theoretical Astrophysics, University of Oslo, PO Box 1029 Blindern, 0315 Oslo, Norway

<sup>19</sup> Departamento de Astronomía, Universidad de Chile, Las Condes, 7591245 Santiago, Chile

<sup>20</sup> Department of Astronomy, School of Science, The University of Tokyo, 7-3-1 Hongo, Bunkyo, Tokyo 113-0033, Japan

<sup>21</sup> Department of Astronomy, Tsinghua University, Beijing 100084, People's Republic of China

<sup>22</sup> Institute for Advanced Study, Kyushu University, Japan

<sup>23</sup> Department of Earth and Planetary Sciences, Faculty of Science, Kyushu University, Nishi-ku, Fukuoka 819-0395, Japan

## ABSTRACT

We present a comprehensive study on the physical and chemical structures of a chemically rich bipolar outflow in a high-mass star forming region IRAS 16272–4837 (SDC335), utilizing high-resolution spectral line data at 1.3 mm and 3 mm dual-bands from the ALMA ATOMS and QUARKS surveys. The high-velocity jet is enveloped by a lower-velocity outflow cavity, containing bright knots that show enhanced molecular intensities and elevated excitation temperatures. Along the outflow, we have identified 35 transitions from 22 molecular species. By analyzing the spatial distribution and kinematics of these molecular lines, we find that the molecular inventory in the outflow is regulated by three processes: (i) direct entrainment from the natal molecular core by the outflow; (ii) shock-induced release of molecules or atoms from dust grains; and (iii) thermal desorption and gas-phase reactions driven by shock heating. These results confirm that outflows are not only dynamical structures but also active chemical factories, where entrainment, shocks, and thermal processing jointly enrich the molecular content. Our findings confirmed that outflow chemistry has multi-origin nature, and provide critical insights into chemical evolution during high-mass star formation.

## 1. INTRODUCTION

Protostellar outflows represent one of the most prominent dynamical phenomena in the early stages of star formation (F. Motte et al. 2018; C.-F. Lee 2020). Outflows are spectroscopically identified by broad high-velocity wings in molecular lines, and spatially by bipolar red- and blue-shifted lobes centered on the protostar. Some outflows exhibit exceptionally rich molecular line emission, including SiO, CH<sub>3</sub>OH, and various sulfur- or nitrogen-bearing molecules. The enhanced abundances of these molecules likely result from non-equilibrium processes induced by shocks, such as ice mantle desorption and grain sputtering (D. Hollenbach & C. F. McKee 1989; D. Flower 1994; B. T. Draine 1995). The chemically enriched regions in these “chemically active outflows” provide a unique laboratory for studying shock-driven chemistry in protostellar environments (M. Tafalla & R. Bachiller 2011; C. Codella et al. 2017; L. Chahine et al. 2024; Y. Oya et al. 2025).

According to current observational and experimental studies, there are two primary mechanisms that can release complex organic molecule (COMs) from the ice mantles into the gas phase – (i) thermal desorption and (ii) dust grain sputtering. In thermal desorption, the ices sublimate at temperatures around 100 K, fully releasing the trapped molecules into the gas phase (L. A. Busch et al. 2022; L. Tychoniec et al. 2021). In such cases, the observed rotational temperatures are typically comparable to or higher than the sublimation threshold ( $\sim$ 100 K). In the latter scenario, sputtering of dust grains requires shock events, which typically occur when the outflowing material collides with the surrounding dense medium at a high speed. These collisions can liberate molecules from the ice mantles into the gas phase (P. Caselli et al. 1997). These shock-induced collisions not only liberate molecules, but also produce line profiles with broad widths and/or high-velocity emission wings. In addition, shocks can heat the ambient material and induce thermal desorption, further enhancing molecular abundances (H. Miura et al. 2017). As the gas cools post-shock, the thermal signature may diminish (T. A. James et al. 2020). Therefore, it is essential to conduct detailed chemical analysis within molecular outflows to distinguish from these two different mechanisms.

In recent years, extensive studies have focused on the chemical characteristics of outflows in low-mass protostars, often inferring excitation mechanisms from velocity-resolved molecular line profiles and revealing that their shock regions can also be chemically rich (H. G. Arce et al. 2008; K. I. Öberg et al. 2011; E. Mendoza et al. 2014; M. De Simone et al. 2020; S. Feng et al. 2020, 2022; S.-Y. Hsu et al. 2024; Y. Chen et al. 2024;

M. Bouvier et al. 2025). For instance, the ASAI survey toward L1157 (B. Lefloch et al. 2018) shows that its two shocked knots (B1 and B2), located  $\sim$ 1.5–2' away from the driving source, exhibit a molecular inventory even richer than the protostar itself, including various COMs (B. Lefloch et al. 2017). In particular, B1 and B2 are among the richest Galactic sources of HNCO and NH<sub>2</sub>CHO, two molecules of prebiotic interest (E. Mendoza et al. 2014). However, previous studies of high-mass protostellar outflows have mostly relied on limited molecular species (e.g., CO and SiO) and often lack spatially resolved kinematic information, which hinders a comprehensive understanding of shock-induced chemistry within these sources (A. Palau et al. 2017; A. Y. Yang et al. 2018; H.-L. Liu et al. 2020b; X. Lu et al. 2021; A. R. Costa Silva et al. 2022; A. Y. Yang et al. 2022; O. S. Rojas-García et al. 2022; J. Xie et al. 2023; L. A. Busch et al. 2024; L. Francis et al. 2024; Y. Xu et al. 2024; O. S. Rojas-García et al. 2024; A. Hoque et al. 2025).

To overcome these limitations, we resolve a chemically rich massive protostellar outflow in the high-mass star-forming region IRDC SDC335.579–0.292 (IRAS 16272–4837, also G335.59-0.29, hereafter SDC335), which is located at a distance of 3.54 kpc. This clump contains a total gas mass of  $\sim$ 3700 M $\odot$  (C. J. Cyganowski et al. 2008; M. Anderson et al. 2021). Within the central region corresponding to the area shown in Figure 1 (b), which encompasses the massive core SDC335-C1, the mass is  $\sim$ 400 M $\odot$  (F. Xu et al. 2023), exhibits high density, and shows chemical richness in COMs such as CH<sub>3</sub>CN, CH<sub>3</sub>OH, CH<sub>3</sub>OCHO, and C<sub>2</sub>H<sub>5</sub>CN (S.-L. Qin et al. 2022; Z.-Y. Li et al. 2025; F. Xu et al. 2024a). It is also associated with a clearly defined bipolar high-velocity outflow (A. Avison et al. 2021), making it an ideal observational platform for exploring non-thermal chemical evolution in high-mass star formation.

In this letter, we report the detection of chemically enriched regions associated with jet-driven shocks in the bipolar molecular outflow of the high-mass protostellar core SDC335 C1, utilizing the wide-band molecular line data at both 3 mm and 1.3 mm bands from the ATOMS-QUARKS survey. Section 2 introduces the two ALMA observations used in this study. Section 3 presents the integrated intensity maps of selected molecular transitions, which reveal chemically enriched zones throughout the bipolar outflow. In Section 4, we further explore the chemical origin of each species within these local regions. Finally, Section 5 summarizes our main findings and conclusions.

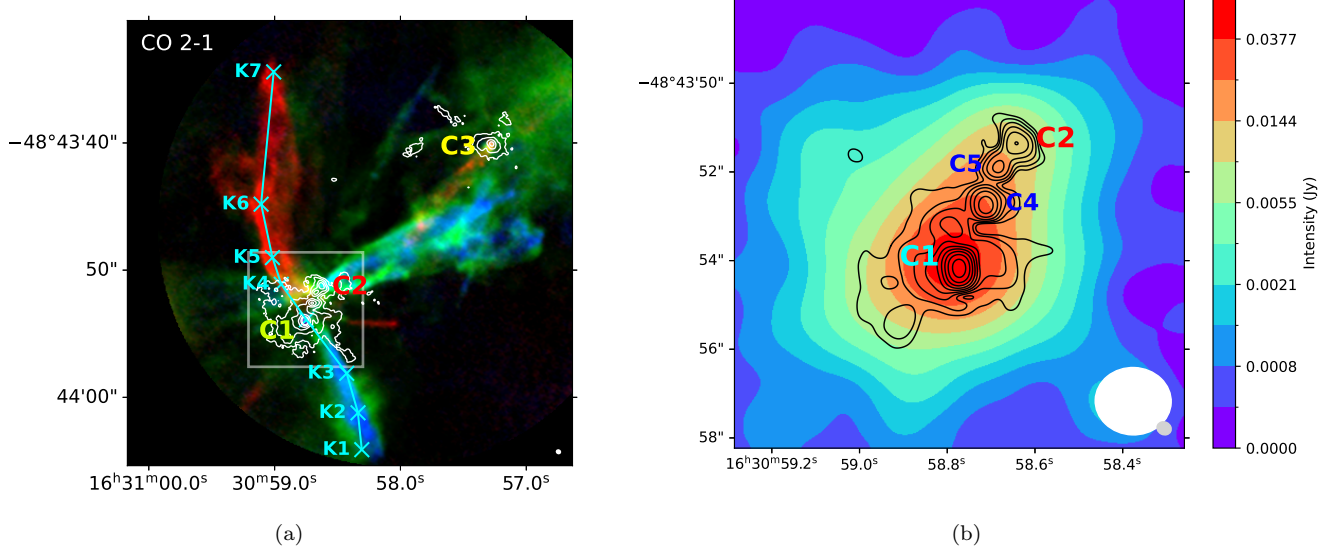


**Figure 1.** (a) CO (2-1) RGB image constructed using the ACA+TM1+TM2 combined data. Blue- and red-shifted components are integrated over velocities of  $-42$  to  $-12$  and  $+12$  to  $+42$   $\text{km s}^{-1}$  relative to the systemic velocity, while the green channel traces emission within  $\pm 12$   $\text{km s}^{-1}$ . The cyan line marks the jet axis. Hot cores C1–C3 and several emission knots are visible. (b) Zoom-in of the central region outlined in (a), with 3 mm continuum in colorscale and 1.3 mm contours highlighting compact sources. Continuum contours start at  $21$   $\text{mJy beam}^{-1}$  and increase in steps of a factor of  $1.618$  (golden ratio). The beams of 3 mm (white) and 1.3 mm (grey) are shown in the lower-right corner.

## 2. OBSERVATIONS

### 2.1. ALMA 3-mm data

We utilized ALMA Band 3 data from the ATOMS survey (Project ID: 2019.1.00685.S; PI: Tie Liu; [T. Liu et al. 2020](#)), which targets 146 massive star-forming clumps using both the 12-m array in C3 configuration and the ACA 7-m array. SDC335 was observed in single-pointing mode, with a spectral setup covering multiple dense gas and shock tracers. In this study, we use the 3 mm continuum map obtained with the 12-m array, which offers higher angular resolution than the ACA-combined data, with a synthesized beam of  $1.7'' \times 1.5''$  and a noise rms of  $10$   $\text{mJy beam}^{-1}$ . We also analyze selected molecular line data from the 12-m + 7-m combined cubes, including transitions of  $\text{HCO}^+(1-0)$ ,  $\text{H}^{13}\text{CO}^+(1-0)$ ,  $\text{SiO}$  (2-1), and  $\text{CH}_3\text{OH}$ , with velocity resolutions of  $0.1$ – $0.2$   $\text{km s}^{-1}$ . More details on the observations and data reduction of this source can be found in [H.-L. Liu et al. 2021](#); [F. Xu et al. 2023](#).

### 2.2. ALMA 1.3-mm data

We also used ALMA Band 6 data from the QUARKS survey (Project ID: 2021.1.00095.S; PIs: Lei Zhu, Guido Garay, and Tie Liu; [X. Liu et al. 2024](#)), which is a high-resolution 1.3 mm follow-up survey of the ATOMS survey. SDC335 was observed using both the 12-m C5 (TM1), 12-m C2 (TM2) and the ACA 7-m arrays, with the best resolution of  $0.3''$  and the maximum recover-

able scale of  $\sim 28''$  ([F. Xu et al. 2024b](#); [D. Yang et al. 2025](#)). In this work, we also used combined TM2 + ACA data for lines because of the higher signal-to-noise ratios at lower resolution. The achieved resolutions of continuum image and line data cube from the TM2 + ACA combined data are approximately  $1.3'' \times 1.1''$ . The noise rms of the continuum image is  $\sim 0.8$   $\text{mJy beam}^{-1}$ . The four spectral windows at 217–221 and 229–233 GHz spectral ranges cover numerous transitions from species such as  $\text{SiO}$  (5–4),  $\text{SO}$  (6–5),  $\text{HNCO}$ ,  $\text{CH}_3\text{OH}$ , and other molecules of interest. The velocity resolution of the line data is about  $1.3$   $\text{km s}^{-1}$ .

## 3. RESULTS

### 3.1. The outflow and driven source

Fig. 1(a) presents the RGB composite image of CO J=2-1 outflows in SDC335, with blue, green, and red colors representing gas velocities blue-shifted by more than  $10$   $\text{km s}^{-1}$ , near the systemic velocity, and red-shifted by more than  $7$   $\text{km s}^{-1}$ , respectively. A bipolar jet-like outflow originates from the core C1, which is identified as the driving source based on its position and chemical richness. The 1.3 mm continuum is overlaid as white contours, and the jet axis, spanning  $\sim 37''$  (0.63 pc at the distance to the source), is indicated by a cyan line. Seven knots marked with “X” correspond to positions along the jet where  $\text{CH}_3\text{OH}$  and  $\text{SiO}$  emission are significantly enhanced in 1.3 mm band (panels iv and xviii

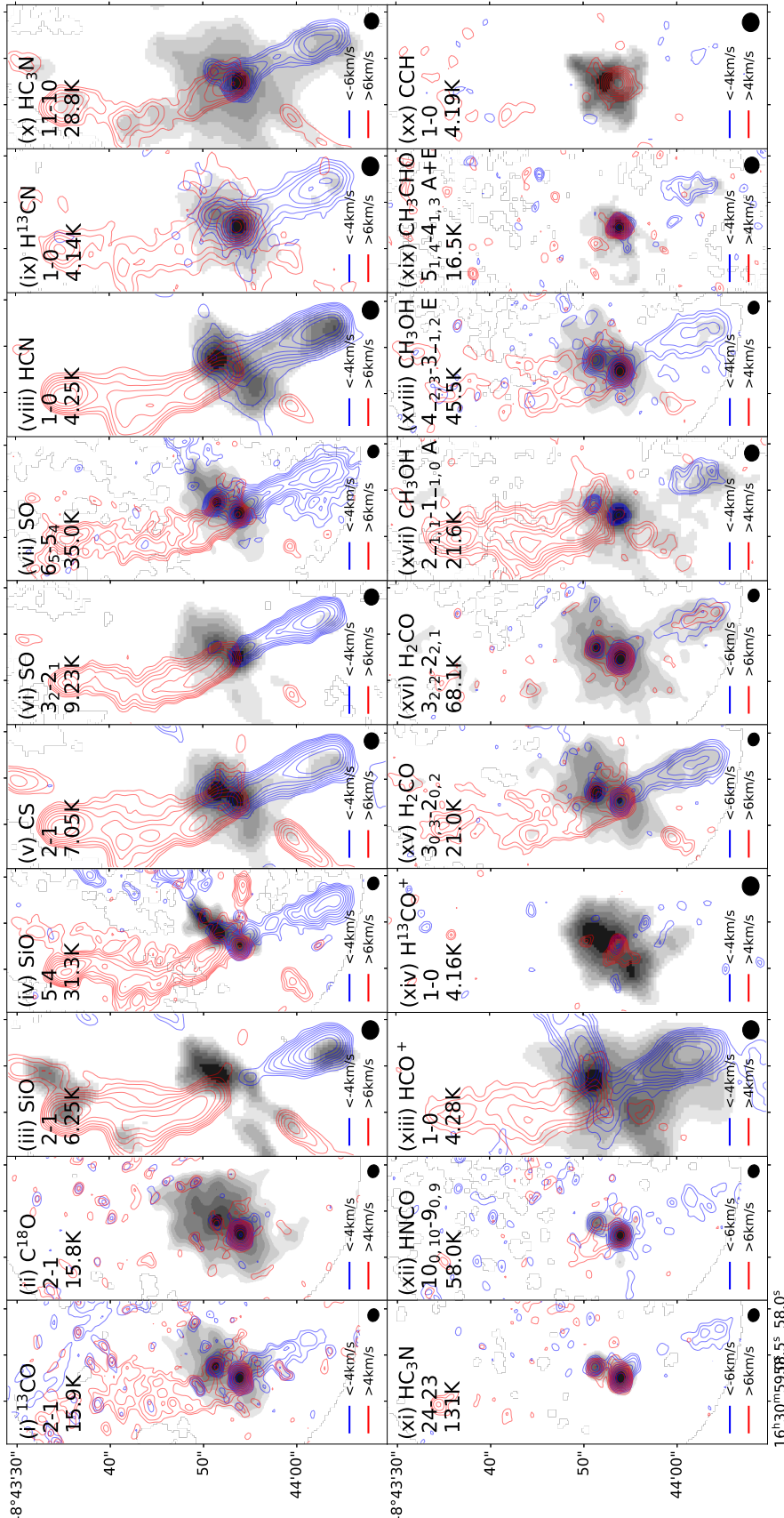


**Figure 2.** Integrated intensity maps of selected molecular transitions detected in SDC335. **Red/Blue contours:** red-shifted and blue-shifted components, with velocity ranges labeled in each panel. **Background:** emission integrated over the systemic velocity gap between the blue- and red-shifted ranges. Contours are drawn at 10 levels logarithmically spaced from  $3\sigma$  to the map maximum. The typical  $1\sigma$  rms in the integrated-intensity maps is  $2.6 \text{ K km s}^{-1}$  for the 3 mm data and  $0.7 \text{ K km s}^{-1}$  for the 1.3 mm data. Each panel lists the corresponding transition and upper energy level.

of Fig. 2). These knots, along with the jet axis, serve as the basis for subsequent analysis and discussion.

Fig. 1(b) shows a zoomed-in view of the white box in panel (a), with the background displaying the 3mm continuum. A low threshold is adopted to highlight the extended warm envelope, while high-threshold black contours of the 1.3mm continuum emphasize compact internal structures. In addition to the three main cores C1, C2, and C3, two earlier-phase cores (C4 and C5) are detected between C1 and C2, consistent with the cores detected in ALMA-DIHCA survey (F. A. Olguin et al. 2021). C1 is a chemically rich core with a deconvolved size of  $1.14'' \times 1.01''$ . In the ATOMS 3mm band survey, 18 COMs were detected toward C1, including  $c$ -C<sub>2</sub>H<sub>4</sub>O, C<sub>2</sub>H<sub>5</sub>CN, CH<sub>3</sub>CHO, and CH<sub>3</sub>OCHO (S.-L. Qin et al. 2022; Z.-Y. Li et al. 2025), indicating that it is a typical hot molecular core. The average line width is  $\sim 4 \text{ km s}^{-1}$ . The non-detection of radio recombination lines (e.g., H30 $\alpha$  or H40 $\alpha$ ) is suggestive of the absence of strong ionized gas emission.

### 3.2. Molecular lines detected along the outflow

We first extracted line spectra at the seven bright knots located along the walls of the jet-driven outflow cavity, where CH<sub>3</sub>OH and SiO emission are significantly enhanced (see Sect. 3.1 and Figs. 1 and 2). To examine their velocity structure at higher spatial resolution, we employed the ACA+TM1+TM2 combined data (see Figs. A1 and A2). Owing to the relatively low signal-to-noise ratio of these data, we integrated every 3 km s<sup>-1</sup> channel to enhance the visibility of extended structures. Given the potential for significant missing flux in the interferometric maps, we did not use these data for quantitative analysis. The resulting channel maps reveal that emission from CO 2–1, SiO 5–4, SO 6<sub>5</sub>–5<sub>4</sub>, H<sub>2</sub>CO 3<sub>0,3</sub>–2<sub>0,2</sub>, and CH<sub>3</sub>OH 4<sub>-2,3</sub>–3<sub>-1,2</sub> is morphologically separated into two kinematic components: a high-velocity ( $> 12 \text{ km s}^{-1}$ ) component concentrated along the collimated outflow axis, and a low-velocity ( $6\text{--}12 \text{ km s}^{-1}$ ) component forming a hollow-shell cavity structure. The seven knots correspond to prominent features in the low-velocity cavity shell, while their high-velocity counterparts trace localized regions along the axis. At a given velocity interval, the spatial distributions of these molecules are broadly similar, with differences mainly in emission strength and the maximum velocity reached—for example, the high-velocity emission of CH<sub>3</sub>OH extends only to  $\sim 21 \text{ km s}^{-1}$ , H<sub>2</sub>CO to  $\sim 24 \text{ km s}^{-1}$ , SO to  $\sim 30 \text{ km s}^{-1}$ , and SiO and CO to  $\sim 33 \text{ km s}^{-1}$ . These differences likely reflect variations in excitation conditions or shock chemistry sensitivity among species. In total, 35 transitions from 22 molec-

ular species were identified at the 3 mm and 1.3 mm bands (see Appendix Table A1).

Fig. 2 presents the integrated intensity maps of 20 representative transitions, with color coding corresponding to blue-shifted, systemic, and red-shifted components. As can be seen in the figure, while most transitions are closely associated with outflow structure, the molecular species exhibit diverse spatial distributions and kinematic properties. For example, H<sup>13</sup>CO<sup>+</sup> and CCH are confined to the quiescent envelope surrounding C1 and C2, characterized by narrow single-peaked profiles (FWHM  $\leq 2 \text{ km s}^{-1}$ ), whereas SiO emission is enhanced at jet-impacted regions and shows broad line wings typical of fast shocks. Similarly, SO displays a spatial and velocity distribution akin to SiO, suggesting both species trace shocked gas. COMs including CH<sub>3</sub>CHO are mainly detected near the outflow termini, indicating sensitivity to local heating or mild shocks. CH<sub>3</sub>OCHO and CH<sub>3</sub>CN are marginally detected and exhibit low S/N as shown in Fig. A2. CH<sub>3</sub>OH emission, although widespread, exhibits relatively weak high-velocity components and is concentrated near the systemic velocity, likely originating from sublimated ices induced by shocks in outflow and the cavity walls.

To further examine the gas kinematics, Fig. 3 presents position–velocity diagrams (PVDs) of several important molecules extracted along the outflow-jet axis (K1–K7, cyan line in Fig. 1(a)). Consistent with the channel maps (Sect. C), the PVDs confirm the morphological separation between high-velocity emission along the axis and low-velocity components in the cavity walls. In addition, the PVDs highlight localized high-velocity peaks at shock positions traced most clearly by SiO and SO, as well as discrete, spatially confined knots in CS, SO, HC<sub>3</sub>N, H<sub>2</sub>CO, and CH<sub>3</sub>OH. These kinematic patterns, combined with the spatial distributions in Fig. 2, reflect diverse excitation mechanisms and physical origins, which will be further analyzed in the following section.

## 4. ANALYSIS AND DISCUSSION

### 4.1. Quantitative Analysis and Global Results

Benefiting from the large number of molecular lines detected across both bands (Section 3.2), we focus on a subset of transitions with sufficiently high S/N for reliable kinematic and excitation analysis. This selection enables a systematic investigation of the physical and chemical origins of the detected species, which we develop in this section.

The channel maps (Section C) reveal a clear separation between high-velocity emission confined to the jet axis and a surrounding low-velocity cavity, with molecule-dependent variations in extent and maximum

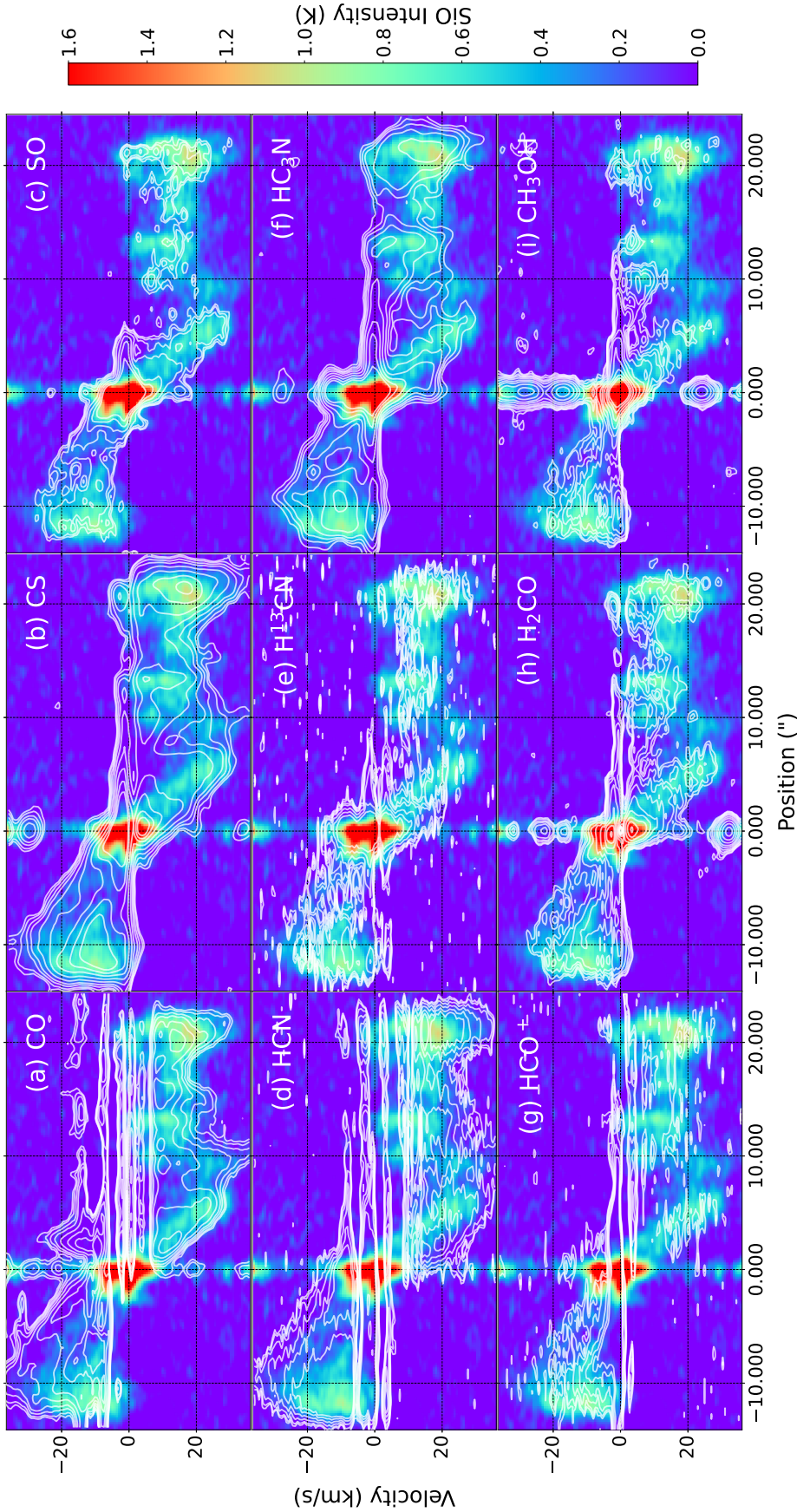


**Figure 3.** PVDs extracted along the jet axis of SDC335. The background color scale in each panel shows SiO emission, tracing the full spatial and velocity extent of the outflow. Overlaid contours correspond to representative transitions of other molecules, as labeled in each panel. Negative offsets indicate the southern (blue-shifted) lobe, and positive offsets indicate the northern (red-shifted) lobe, with  $0''$  marking the C1.

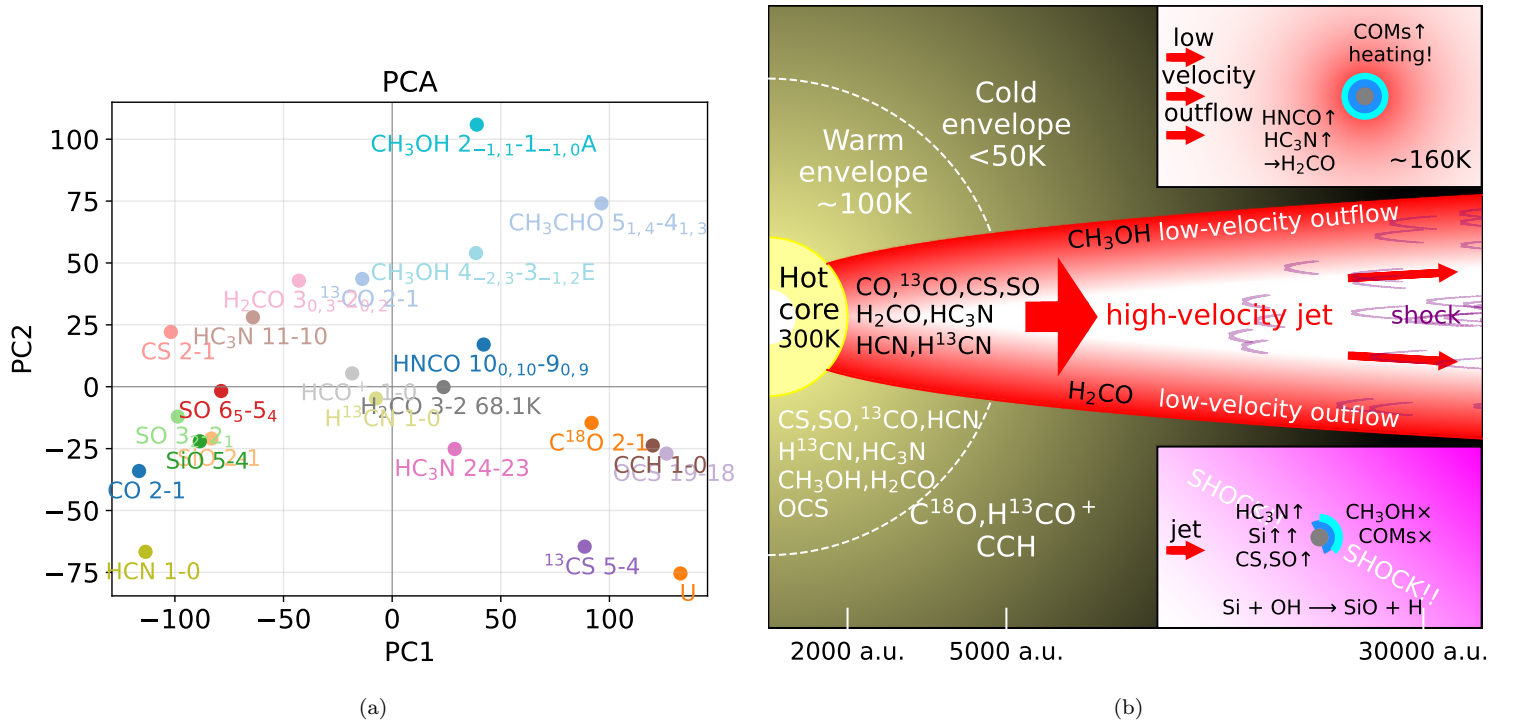


**Figure 4.** (a) PCA of molecular emission along the jet axis (data within  $\pm 2''$  of C1 excluded). Molecules are separated into four quadrants reflecting dominant chemical-kinematic behavior: Quadrant I: COMs enhanced in shocked regions; Quadrant II: outflow tracers with low- and high-velocity components; Quadrant III: shock/high-velocity tracers; Quadrant IV: systemic-velocity or low S/N lines. (b) Schematic view of the physical and chemical structure of the bipolar outflow in SDC335. The main panel shows the spatial distribution of key molecular tracers associated with the hot core, warm envelope, and jet-driven outflows. The upper inset illustrates post-shock low-velocity outflows heating the gas and sublimating molecules from icy mantles. The lower inset depicts strong shocks destroying dust grains, releasing ice-phase material and driving Si atoms from grain cores into the gas phase to form SiO.

## Pairwise Molecular Correlation (Kendall)

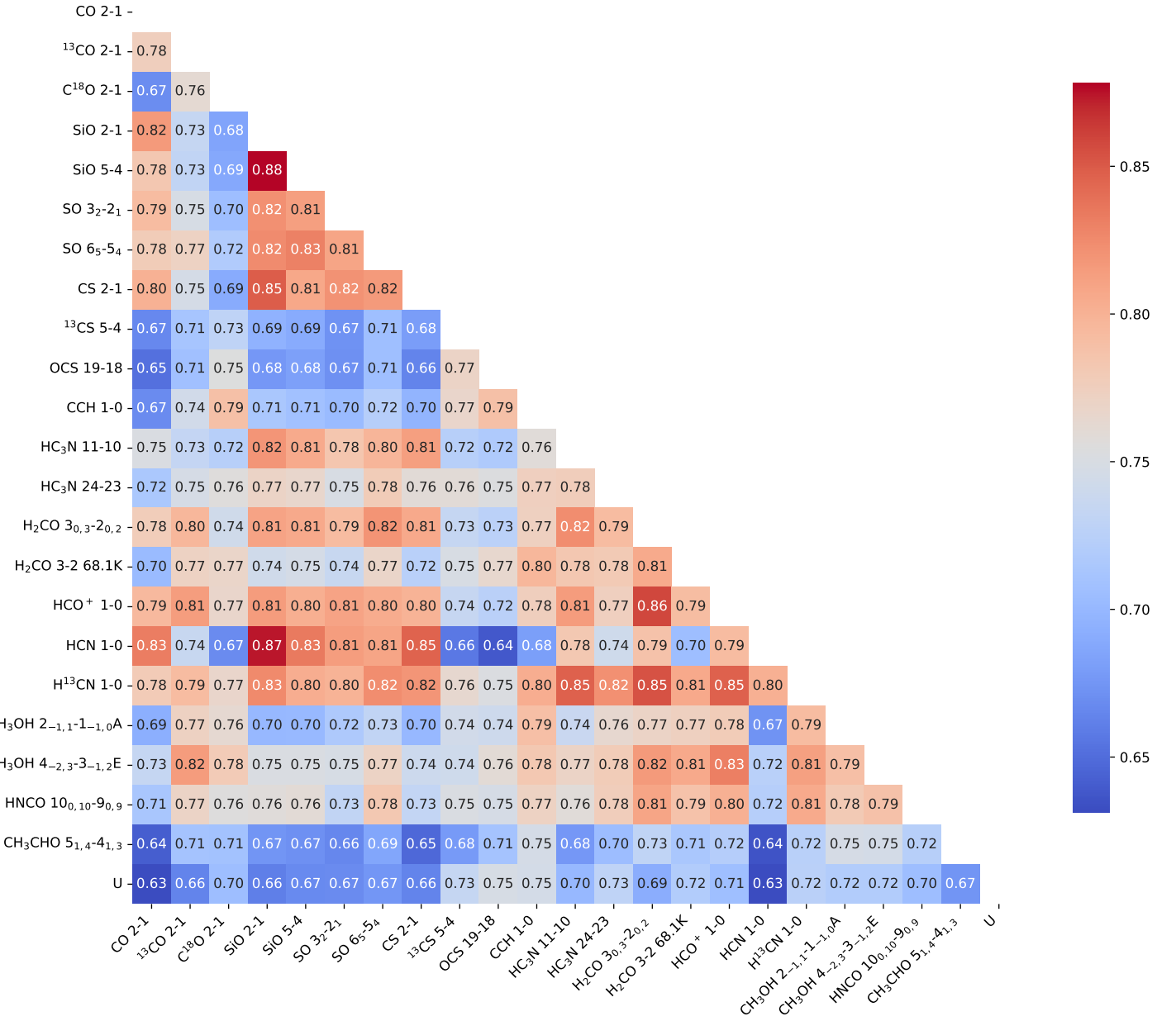


**Figure 5.** Kendall rank correlation coefficients between integrated intensities of molecular lines, shown as a lower-triangular matrix to avoid duplication.

velocity. Consistently, the PVD (Fig.3) and moment0 map (Fig.2) show that the bipolar jet driven by C1 is remarkably symmetric within  $\pm 14''$  in both morphology and velocity, reaching line-of-sight velocities of up to  $\pm 40 \text{ km s}^{-1}$  at  $\sim \pm 10''$  from C1. The broadest line widths (up to  $20 \text{ km s}^{-1}$ ) and the highest gas temperatures are found at knots K1, K6, and K7, coinciding with peaks in molecular emission. Independent constraints from H<sub>2</sub>CO rotational analysis (Fig. B4) reveal  $T_{\text{rot}} \gtrsim 200 \text{ K}$  at several knots, consistent with strong

shock heating by the protostellar jet and suggesting that multiple chemical processes—direct entrainment, shock sputtering, and thermal desorption—operate simultaneously along the outflow.

To quantify chemical variations, we computed position-integrated intensities of multiple transitions along the jet axis (Fig.B1). Assuming LTE and optically thin conditions, these serve as proxies for column densities. Most molecules, except  $^{13}\text{CO}$  and  $\text{C}^{18}\text{O}$ , show enhancements near K1-K7. Using  $^{13}\text{CO}$  as a tracer of H<sub>2</sub>

column density, relative intensity ratios (Fig. B2) highlight localized abundance peaks at the knots.

Spectral profiles provide complementary constraints (Fig. B5). Molecules linked to shocks, such as SiO, SO, and HCN, display broad wings and strong high-velocity components, whereas CH<sub>3</sub>CHO and CH<sub>3</sub>CN peak near the systemic velocity with weak wings. These differences reflect distinct excitation and formation pathways, consistent with the spatial–kinematic separation observed in the channel maps and PVDs.

Building on these diagnostics—integrated intensity (Fig. B2), line profile (Fig. B5), and the ratio of systemic-to non-systemic-velocity components (Fig. 2)—we performed PCA on the molecular PVDs (Fig. 4(a)). This separates molecules into four groups, consistent with Section 4.2:

- Quadrant I (Sec. 4.2.3): COMs, concentrated near systemic velocity but enhanced in terminal knots, reflecting ice-mantle sublimation and gas-phase reactions;
- Quadrant II (Sec. 4.2.1): outflow tracers spanning low- and high-velocity components, with stable intensities from the hot core outward, indicative of entrained ambient gas;
- Quadrant III (Sec. 4.2.2): species associated with shocks or high-velocity jets, peaking at terminal knots where collisions produce strong shocks;
- Quadrant IV: molecules dominated by systemic-velocity emission or with low S/N, weakly affected by jet-induced shocks or of uncertain origin.

Finally, PCA on the full 18,684-dimensional vectors (173 positions  $\times$  108 high-velocity channels) shows that PC1 and PC2 account for 36.2% and 10.3% of the variance (46.5% combined), with nearly all variance driven by spatial differences in high-velocity ( $> 4 \text{ km s}^{-1}$ ) line intensities.

Complementing this, pairwise Kendall correlations (Fig. 5) reveal that CS, SO, HCN, and SiO are tightly correlated ( $> 0.8$ ), with the strongest correlation (0.88) between two SiO transitions  $J=2-1$  and  $J=5-4$ . H<sub>2</sub>CO and HCO<sup>+</sup> correlate uniformly with most species (0.77–0.83) and with each other (0.86), indicating strong chemical coupling. Notably, CH<sub>3</sub>OH  $2_{-1,1}-1_{-1,0}$  A and  $4_{-2,3}-3_{-1,2}$  E correlate at only 0.79, and their correlations with other molecules show larger differences, possibly related to nuclear spin isomers (Zou et al., in prep.).

The results are also illustrated in a schematic cartoon (Fig. 4 (b)). We emphasize that the PCA quadrants indicate the dominant origin of each molecule along the

jet, but many molecules can have contributions from more than one source. This motivates the detailed classification and discussion in the following subsections.

## 4.2. Classification of Molecules

### 4.2.1. Molecules Entrained by the Outflow

This group comprises molecules that are abundant in the dense core and are primarily carried outward by the jet-driven outflow, including CO, <sup>13</sup>CO, HCO<sup>+</sup>, H<sub>2</sub>CO, CS, and HC<sub>3</sub>N. As shown in the channel maps (Fig. C1, C5) and PVDs (Fig. 3), these species are detected both along the collimated jet axis and within the surrounding cavity-like low-velocity structures. Their line profiles (Appendix Fig. B5) generally display broad wings together with systemic or intermediate-velocity components, indicating that they mainly trace gas physically entrained and dynamically processed by the jet–ambient interaction (M. Tafalla et al. 2010; B. Tabone et al. 2020; L. Podio et al. 2021; L. Tychoniec et al. 2019).

Relative intensity ratios to <sup>13</sup>CO (Appendix Fig. B2, B3) remain nearly flat in regions lacking strong shocks, but show moderate enhancements at bright knots. Within this set, CO and HCO<sup>+</sup> are canonical tracers of entrained gas; H<sub>2</sub>CO can be supplied by gas-phase formation and/or non-thermal release from grains (L. Tychoniec et al. 2019); CS and HC<sub>3</sub>N follow the same spatial–kinematic pattern and predominantly trace dense gas swept up by the outflow.

### 4.2.2. Molecules Released into the Gas Phase by Jet-Induced Shocks

A second group of molecules shows clear evidence of shock-related enhancement, including SiO, SO, HCN (and its isotopologues H<sup>13</sup>CN and DCN), HC<sub>3</sub>N, and HC<sub>3</sub>N. Channel maps and PVDs (Figs. C3, C4, and 3) reveal that their emissions are concentrated along the jet axis and peak at bright knots, with broad wings and high-velocity components comparable to SiO (Appendix Fig. B5). Their intensity ratios relative to <sup>13</sup>CO also rise sharply at these knots (Appendix Fig. B2), confirming that they trace material chemically reprocessed in shocks.

In cold dense clouds, Si is locked in dust grains and SiO is therefore heavily depleted (S. Guilloteau et al. 1992; A. Dutrey et al. 1997). Jet-induced shocks liberate Si atoms via non-thermal sputtering or grain fragmentation, which then react with OH or O to form SiO (P. Caselli et al. 1997; P. Schilke et al. 1997; A. Gusdorf et al. 2008a,b). Such localized SiO emission has been widely observed in sources such as TMC1, SMM3, and HH 211 (L. Podio et al. 2015; N. Sakai et al. 2014; L. Tychoniec et al. 2019).

SO chemistry is likewise tied to shocks: sulfur released from grains can react with OH or O to form SO (T. W. Hartquist et al. 1980; T. J. Millar & D. A. Williams 1993), while high-temperature reactions involving H<sub>2</sub>S further enhance SO abundance in fast shocks where OH and O abundances increase sharply (A. Gusdorf et al. 2008b). Although slower shocks can also contribute, the strongest SO emission is typically found in energetic jet–ambient collisions.

HCN and its isotopologues (H<sup>13</sup>CN, DCN) exhibit SiO-like kinematics in our data. Their enhancement can be explained by gas-phase reactions of CN with H<sub>2</sub> in warm post-shock gas (S. Bruderer et al. 2009; R. Visser et al. 2018). In HH211, H<sup>13</sup>CN has been observed tracing cavity walls, supporting a scenario where UV irradiation and high-temperature chemistry act in tandem (L. Tychoniec et al. 2019).

Although HC<sub>3</sub>N is often regarded as a more complex N-bearing molecule, it likewise shows signs of shock enhancement (X. Lu et al. 2021; A. Hoque et al. 2025). Possible formation pathways include polymerization of CN intermediates or release of atomic N in nitrogen-rich, low C/O environments (J. K. Jørgensen et al. 2004; C. Codella et al. 2009, 2010). An additional efficient gas-phase route is the reaction C<sub>2</sub>H<sub>2</sub> + CN → HC<sub>3</sub>N + H (K. Fukuzawa & Y. Osamura 1997; J. F. Chapman et al. 2009; E. Mendoza et al. 2018), which becomes more active in shocked gas.

Overall, the enhancement of these molecules is best understood through two complementary processes:

- (i) **sputtering of atoms or molecules** (e.g., Si, S, HCN) from dust grains into the gas phase, and
- (ii) **rapid activation of high-temperature chemistry** at shock fronts, producing additional N- and O-bearing species.

#### 4.2.3. *Molecules Thermally Excited by Shock Heating in the Jet*

A third group of molecules shows enhanced abundances that are best explained by shock-induced heating rather than direct sputtering. Channel maps and PVDs (Figs. C6, 3) reveal that their emissions peak at the systemic velocity of the outflow, while intensity ratios relative to <sup>13</sup>CO still increase at bright knots (Appendix Fig. B2). Line profiles (Appendix Fig. B5) confirm that CH<sub>3</sub>OH and HNCO sometimes display additional broad wings tracing the outflow, whereas CH<sub>3</sub>CHO, CH<sub>3</sub>CN, and CH<sub>3</sub>OCHO are confined to narrow systemic components. This pattern, combined with the correlation between SiO gradients and H<sub>2</sub>CO rotational temperatures derived with RADEX (T. Möller et al. 2017) following

methods similar to N. Izumi et al. (2024) (Fig. B4), indicates excitation primarily driven by local thermal heating in shocked gas.

The observed enhancements can be attributed to high-temperature gas-phase chemistry coupled with thermal desorption of icy mantles. CH<sub>3</sub>OH, for example, forms efficiently on grain surfaces at low temperatures and is readily released into the gas phase by heating (N. Watanabe et al. 2004; K. I. Öberg et al. 2009). Other species such as CH<sub>3</sub>CHO and HNCO are likewise desorbed or reprocessed through high-temperature reactions in shocked zones (A. Bacmann et al. 2012; S. Scibelli & Y. Shirley 2020). Comparisons with hot cores, such as S68N (M. L. van Gelder et al. 2020; P. Nazari et al. 2021), show similar abundance ratios, suggesting shared thermal histories or transient regeneration in shocks. Observations in L1157-B1 and SMM3 further support this scenario, where localized heating can mimic hot-core conditions and temporarily enable the release or synthesis of complex organics (M. De Simone et al. 2020; L. Tychoniec et al. 2021).

In summary, the elevated abundances of CH<sub>3</sub>OH, HNCO, and several COMs are mainly attributed to high temperatures induced by jet–ambient shocks. Thermal desorption and rapid gas-phase chemistry work in concert, enhancing molecular complexity in the outflow beyond that expected from the hot core alone.

Overall, our classification highlights the predominant behaviors of different molecular groups—entrainment from the core, shock-induced release, and thermal excitation by heating. However, these categories should not be regarded as mutually exclusive. As shown in Fig. 5 and Fig. 4, some molecules exhibit stronger correlations across groups than within their assigned category, underscoring the complexity of chemical processes in jet–outflow systems. This scheme therefore provides a useful framework for interpretation, but the role of each molecule may vary with local physical conditions, and caution is warranted when drawing sharp boundaries between categories.

## 5. CONCLUSIONS

We have presented ALMA observations of the chemically rich jet and outflow system in SDC335, detecting 35 transitions from 22 molecular species. By extracting channel maps, PVDs, integrated intensity ratios, and line profiles, we conducted a quantitative analysis of the spatial–kinematic and excitation properties of different molecules.

Principal component analysis (PCA) of these parameters shows that line profiles provide the largest variance among species, serving as the dominant feature

distinguishing their behaviors. The PCA distribution naturally separates molecules into three quadrants, corresponding to three predominant classes: (1) species entrained from the dense core by the outflow (e.g., CO, HCO<sup>+</sup>, CS, HC<sub>3</sub>N); (2) molecules released into the gas phase or newly formed in jet-induced shocks (e.g., SiO, SO, HCN, DCN); and (3) molecules thermally excited by shock heating and subsequent gas-phase or desorption processes (e.g., CH<sub>3</sub>OH, CH<sub>3</sub>CHO, CH<sub>3</sub>CN, HNCO, CH<sub>3</sub>OCHO). These groups display distinct spatial-kinematic signatures, with entrained tracers extended along the cavity walls, shock tracers peaking at high-velocity knots, and thermally excited species confined to systemic-velocity components with local enhancements at knots. However, individual species may participate in multiple processes—entrainment, sputtering, or thermal heating—depending on local conditions. The observed chemistry of the outflow is therefore shaped by the interplay of all three mechanisms rather than by a single pathway.

In summary, our study highlights the multi-origin nature of molecular emission in a massive protostellar outflow, combining entrainment from the core, shock-driven release, and thermal excitation by shock heating. Future observations with higher angular resolution and sensitivity, together with laboratory and modeling efforts on grain-surface and gas-phase chemistry under shock con-

ditions, will be essential to disentangle the relative contributions of these processes and to quantify the physical-chemical environment of massive outflows.

## ACKNOWLEDGMENTS

Tie Liu acknowledges the supports by the National Key R&D Program of China (No. 2022YFA1603101), National Natural Science Foundation of China (NSFC) through grants No.12073061 and No.12122307, the PIFI program of Chinese Academy of Sciences through grant No. 2025PG0009, and the Tianchi Talent Program of Xinjiang Uygur Autonomous Region.

H.-L. Liu is supported by Yunnan Fundamental Research Project (grant No. 202301AT070118, 202401AS070121), and by Xingdian Talent Support Plan—Youth Project.

A.H. thank the support of the S. N. Bose National Centre for Basic Sciences under the Department of Science and Technology, Govt. of India and the CSIR-HRDG, Govt. of India for funding the fellowship.

SRD acknowledges support from the Fondecyt Postdoctoral fellowship (project code 3220162) and ANID BASAL project FB210003.

*Facilities:* ALMA

## REFERENCES

Anderson, M., Peretto, N., Ragan, S. E., et al. 2021, MNRAS, 508, 2964, doi: [10.1093/mnras/stab2674](https://doi.org/10.1093/mnras/stab2674)

Arce, H. G., Santiago-García, J., Jørgensen, J. K., Tafalla, M., & Bachiller, R. 2008, ApJL, 681, L21, doi: [10.1086/590110](https://doi.org/10.1086/590110)

Avison, A., Fuller, G. A., Peretto, N., et al. 2021, A&A, 645, A142, doi: [10.1051/0004-6361/201936043](https://doi.org/10.1051/0004-6361/201936043)

Bacmann, A., Taquet, V., Faure, A., Kahane, C., & Ceccarelli, C. 2012, A&A, 541, L12, doi: [10.1051/0004-6361/201219207](https://doi.org/10.1051/0004-6361/201219207)

Bouvier, M., Giani, L., Chahine, L., et al. 2025, MNRAS, 539, 2380, doi: [10.1093/mnras/staf631](https://doi.org/10.1093/mnras/staf631)

Bruderer, S., Benz, A. O., Bourke, T. L., & Doty, S. D. 2009, A&A, 503, L13, doi: [10.1051/0004-6361/200912620](https://doi.org/10.1051/0004-6361/200912620)

Busch, L. A., Belloche, A., Garrod, R. T., Müller, H. S. P., & Menten, K. M. 2022, A&A, 665, A96, doi: [10.1051/0004-6361/202243383](https://doi.org/10.1051/0004-6361/202243383)

Busch, L. A., Belloche, A., Garrod, R. T., Müller, H. S. P., & Menten, K. M. 2024, A&A, 681, A104, doi: [10.1051/0004-6361/202347256](https://doi.org/10.1051/0004-6361/202347256)

Caselli, P., Hartquist, T. W., & Havnes, O. 1997, A&A, 322, 296

Chahine, L., Ceccarelli, C., De Simone, M., et al. 2024, MNRAS, 531, 2653, doi: [10.1093/mnras/stae1320](https://doi.org/10.1093/mnras/stae1320)

Chapman, J. F., Millar, T. J., Wardle, M., Burton, M. G., & Walsh, A. J. 2009, MNRAS, 394, 221, doi: [10.1111/j.1365-2966.2008.14144.x](https://doi.org/10.1111/j.1365-2966.2008.14144.x)

Chen, Y., Rocha, W. R. M., van Dishoeck, E. F., et al. 2024, A&A, 690, A205, doi: [10.1051/0004-6361/202450706](https://doi.org/10.1051/0004-6361/202450706)

Codella, C., Benedettini, M., Beltrán, M. T., et al. 2009, A&A, 507, L25, doi: [10.1051/0004-6361/200913340](https://doi.org/10.1051/0004-6361/200913340)

Codella, C., Lefloch, B., Ceccarelli, C., et al. 2010, A&A, 518, L112, doi: [10.1051/0004-6361/201014582](https://doi.org/10.1051/0004-6361/201014582)

Codella, C., Ceccarelli, C., Caselli, P., et al. 2017, A&A, 605, L3, doi: [10.1051/0004-6361/201731249](https://doi.org/10.1051/0004-6361/201731249)

Costa Silva, A. R., Fedriani, R., Tan, J. C., et al. 2022, A&A, 659, A23, doi: [10.1051/0004-6361/202142412](https://doi.org/10.1051/0004-6361/202142412)

Cyganowski, C. J., Whitney, B. A., Holden, E., et al. 2008, AJ, 136, 2391, doi: [10.1088/0004-6256/136/6/2391](https://doi.org/10.1088/0004-6256/136/6/2391)

De Simone, M., Codella, C., Ceccarelli, C., et al. 2020, *A&A*, 640, A75, doi: [10.1051/0004-6361/201937004](https://doi.org/10.1051/0004-6361/201937004)

Draine, B. T. 1995, *Ap&SS*, 233, 111, doi: [10.1007/BF00627339](https://doi.org/10.1007/BF00627339)

Dutrey, A., Guilloteau, S., & Bachiller, R. 1997, *A&A*, 325, 758

Feng, S., Liu, H. B., Caselli, P., et al. 2022, *ApJL*, 933, L35, doi: [10.3847/2041-8213/ac75d7](https://doi.org/10.3847/2041-8213/ac75d7)

Feng, S., Codella, C., Ceccarelli, C., et al. 2020, *ApJ*, 896, 37, doi: [10.3847/1538-4357/ab8813](https://doi.org/10.3847/1538-4357/ab8813)

Flower, D. 1994, in *Astronomical Society of the Pacific Conference Series*, Vol. 58, The First Symposium on the Infrared Cirrus and Diffuse Interstellar Clouds, ed. R. M. Cutri & W. B. Latter, 332

Francis, L., van Gelder, M. L., van Dishoeck, E. F., et al. 2024, *A&A*, 683, A249, doi: [10.1051/0004-6361/202348105](https://doi.org/10.1051/0004-6361/202348105)

Fukuzawa, K., & Osamura, Y. 1997, *ApJ*, 489, 113, doi: [10.1086/304782](https://doi.org/10.1086/304782)

Guilloteau, S., Bachiller, R., Fuente, A., & Lucas, R. 1992, *A&A*, 265, L49

Gusdorf, A., Cabrit, S., Flower, D. R., & Pineau Des Forêts, G. 2008a, *A&A*, 482, 809, doi: [10.1051/0004-6361:20078900](https://doi.org/10.1051/0004-6361:20078900)

Gusdorf, A., Pineau Des Forêts, G., Cabrit, S., & Flower, D. R. 2008b, *A&A*, 490, 695, doi: [10.1051/0004-6361:200810443](https://doi.org/10.1051/0004-6361:200810443)

Hartquist, T. W., Dalgarno, A., & Oppenheimer, M. 1980, *ApJ*, 236, 182, doi: [10.1086/157731](https://doi.org/10.1086/157731)

Hollenbach, D., & McKee, C. F. 1989, *ApJ*, 342, 306, doi: [10.1086/167595](https://doi.org/10.1086/167595)

Hoque, A., Baug, T., Dewangan, L. K., et al. 2025, *The Astrophysical Journal*, 987, 197, doi: [10.3847/1538-4357/add928](https://doi.org/10.3847/1538-4357/add928)

Hsu, S.-Y., Lee, C.-F., Liu, S.-Y., et al. 2024, *ApJ*, 976, 29, doi: [10.3847/1538-4357/ad7e25](https://doi.org/10.3847/1538-4357/ad7e25)

Izumi, N., Sanhueza, P., Koch, P. M., et al. 2024, *ApJ*, 963, 163, doi: [10.3847/1538-4357/ad18c6](https://doi.org/10.3847/1538-4357/ad18c6)

James, T. A., Viti, S., Holdship, J., & Jiménez-Serra, I. 2020, *A&A*, 634, A17, doi: [10.1051/0004-6361/201936536](https://doi.org/10.1051/0004-6361/201936536)

Jørgensen, J. K., Hogerheijde, M. R., Blake, G. A., et al. 2004, *A&A*, 415, 1021, doi: [10.1051/0004-6361:20034216](https://doi.org/10.1051/0004-6361:20034216)

Lee, C.-F. 2020, *A&A Rv*, 28, 1, doi: [10.1007/s00159-020-0123-7](https://doi.org/10.1007/s00159-020-0123-7)

Lefloch, B., Ceccarelli, C., Codella, C., et al. 2017, *MNRAS*, 469, L73, doi: [10.1093/mnrasl/slx050](https://doi.org/10.1093/mnrasl/slx050)

Lefloch, B., Bachiller, R., Ceccarelli, C., et al. 2018, *MNRAS*, 477, 4792, doi: [10.1093/mnras/sty937](https://doi.org/10.1093/mnras/sty937)

Li, Z.-Y., Liu, X., Liu, T., et al. 2025, *A&A*, 697, A190, doi: [10.1051/0004-6361/202452762](https://doi.org/10.1051/0004-6361/202452762)

Liu, H.-L., Sanhueza, P., Liu, T., et al. 2020b, *ApJ*, 901, 31, doi: [10.3847/1538-4357/abadfe](https://doi.org/10.3847/1538-4357/abadfe)

Liu, H.-L., Liu, T., Evans, Neal J., I., et al. 2021, *MNRAS*, 505, 2801, doi: [10.1093/mnras/stab1352](https://doi.org/10.1093/mnras/stab1352)

Liu, T., Evans, N. J., Kim, K.-T., et al. 2020, *MNRAS*, 496, 2790, doi: [10.1093/mnras/staa1577](https://doi.org/10.1093/mnras/staa1577)

Liu, X., Liu, T., Zhu, L., et al. 2024, *Research in Astronomy and Astrophysics*, 24, 025009, doi: [10.1088/1674-4527/ad0d5c](https://doi.org/10.1088/1674-4527/ad0d5c)

Lu, X., Li, S., Ginsburg, A., et al. 2021, *ApJ*, 909, 177, doi: [10.3847/1538-4357/abde3c](https://doi.org/10.3847/1538-4357/abde3c)

Mendoza, E., Lefloch, B., López-Sepulcre, A., et al. 2014, *MNRAS*, 445, 151, doi: [10.1093/mnras/stu1718](https://doi.org/10.1093/mnras/stu1718)

Mendoza, E., Lefloch, B., Ceccarelli, C., et al. 2018, *MNRAS*, 475, 5501, doi: [10.1093/mnras/sty180](https://doi.org/10.1093/mnras/sty180)

Millar, T. J., & Williams, D. A. 1993, *Dust and chemistry in astronomy*

Miura, H., Yamamoto, T., Nomura, H., et al. 2017, *ApJ*, 839, 47, doi: [10.3847/1538-4357/aa67df](https://doi.org/10.3847/1538-4357/aa67df)

Möller, T., Endres, C., & Schilke, P. 2017, *A&A*, 598, A7, doi: [10.1051/0004-6361/201527203](https://doi.org/10.1051/0004-6361/201527203)

Motte, F., Bontemps, S., & Louvet, F. 2018, *ARA&A*, 56, 41, doi: [10.1146/annurev-astro-091916-055235](https://doi.org/10.1146/annurev-astro-091916-055235)

Nazari, P., van Gelder, M. L., van Dishoeck, E. F., et al. 2021, *A&A*, 650, A150, doi: [10.1051/0004-6361/202039996](https://doi.org/10.1051/0004-6361/202039996)

Öberg, K. I., Garrod, R. T., van Dishoeck, E. F., & Linnartz, H. 2009, *A&A*, 504, 891, doi: [10.1051/0004-6361/200912559](https://doi.org/10.1051/0004-6361/200912559)

Öberg, K. I., van der Marel, N., Kristensen, L. E., & van Dishoeck, E. F. 2011, *ApJ*, 740, 14, doi: [10.1088/0004-637X/740/1/14](https://doi.org/10.1088/0004-637X/740/1/14)

Olguin, F. A., Sanhueza, P., Guzmán, A. E., et al. 2021, *ApJ*, 909, 199, doi: [10.3847/1538-4357/abde3f](https://doi.org/10.3847/1538-4357/abde3f)

Oya, Y., Saiga, E., Miotello, A., et al. 2025, *ApJ*, 980, 263, doi: [10.3847/1538-4357/adabe7](https://doi.org/10.3847/1538-4357/adabe7)

Palau, A., Walsh, C., Sánchez-Monge, Á., et al. 2017, *MNRAS*, 467, 2723, doi: [10.1093/mnras/stx004](https://doi.org/10.1093/mnras/stx004)

Podio, L., Codella, C., Gueth, F., et al. 2015, *A&A*, 581, A85, doi: [10.1051/0004-6361/201525778](https://doi.org/10.1051/0004-6361/201525778)

Podio, L., Tabone, B., Codella, C., et al. 2021, *A&A*, 648, A45, doi: [10.1051/0004-6361/202038429](https://doi.org/10.1051/0004-6361/202038429)

Qin, S.-L., Liu, T., Liu, X., et al. 2022, *MNRAS*, 511, 3463, doi: [10.1093/mnras/stac219](https://doi.org/10.1093/mnras/stac219)

Rojas-García, O. S., Gómez-Ruiz, A. I., Palau, A., et al. 2022, *ApJS*, 262, 13, doi: [10.3847/1538-4365/ac81cb](https://doi.org/10.3847/1538-4365/ac81cb)

Rojas-García, O. S., Gómez-Ruiz, A. I., Palau, A., et al. 2024, *MNRAS*, 527, 2110, doi: [10.1093/mnras/stad3161](https://doi.org/10.1093/mnras/stad3161)

Sakai, N., Sakai, T., Hirota, T., et al. 2014, *Nature*, 507, 78, doi: [10.1038/nature13000](https://doi.org/10.1038/nature13000)

Schilke, P., Walmsley, C. M., Pineau des Forets, G., & Flower, D. R. 1997, *A&A*, 321, 293

Scibelli, S., & Shirley, Y. 2020, *ApJ*, 891, 73, doi: [10.3847/1538-4357/ab7375](https://doi.org/10.3847/1538-4357/ab7375)

Tabone, B., Godard, B., Pineau des Forêts, G., Cabrit, S., & van Dishoeck, E. F. 2020, *A&A*, 636, A60, doi: [10.1051/0004-6361/201937383](https://doi.org/10.1051/0004-6361/201937383)

Tafalla, M., & Bachiller, R. 2011, in IAU Symposium, Vol. 280, The Molecular Universe, ed. J. Cernicharo & R. Bachiller, 88–102, doi: [10.1017/S1743921311024896](https://doi.org/10.1017/S1743921311024896)

Tafalla, M., Santiago-García, J., Hacar, A., & Bachiller, R. 2010, *A&A*, 522, A91, doi: [10.1051/0004-6361/201015158](https://doi.org/10.1051/0004-6361/201015158)

Tychoniec, L., Hull, C. L. H., Kristensen, L. E., et al. 2019, *A&A*, 632, A101, doi: [10.1051/0004-6361/201935409](https://doi.org/10.1051/0004-6361/201935409)

Tychoniec, L., van Dishoeck, E. F., van't Hoff, M. L. R., et al. 2021, *A&A*, 655, A65, doi: [10.1051/0004-6361/202140692](https://doi.org/10.1051/0004-6361/202140692)

van der Tak, F. F. S., Black, J. H., Schöier, F. L., Jansen, D. J., & van Dishoeck, E. F. 2007, *A&A*, 468, 627, doi: [10.1051/0004-6361:20066820](https://doi.org/10.1051/0004-6361:20066820)

van Gelder, M. L., Tabone, B., Tychoniec, L., et al. 2020, *A&A*, 639, A87, doi: [10.1051/0004-6361/202037758](https://doi.org/10.1051/0004-6361/202037758)

Visser, R., Bruderer, S., Cazzoletti, P., et al. 2018, *A&A*, 615, A75, doi: [10.1051/0004-6361/201731898](https://doi.org/10.1051/0004-6361/201731898)

Watanabe, N., Nagaoka, A., Shiraki, T., & Kouchi, A. 2004, *ApJ*, 616, 638, doi: [10.1086/424815](https://doi.org/10.1086/424815)

Xie, J., Li, J., Wang, J., et al. 2023, *ApJ*, 949, 89, doi: [10.3847/1538-4357/acc83f](https://doi.org/10.3847/1538-4357/acc83f)

Xu, F., Wang, K., Liu, T., et al. 2023, *MNRAS*, 520, 3259, doi: [10.1093/mnras/stad012](https://doi.org/10.1093/mnras/stad012)

Xu, F., Wang, K., Liu, T., et al. 2024a, *ApJS*, 270, 9, doi: [10.3847/1538-4365/acfee5](https://doi.org/10.3847/1538-4365/acfee5)

Xu, F., Wang, K., Liu, T., et al. 2024b, *Research in Astronomy and Astrophysics*, 24, 065011, doi: [10.1088/1674-4527/ad3dc3](https://doi.org/10.1088/1674-4527/ad3dc3)

Xu, Y., Wang, J., Liu, S., et al. 2024, *AJ*, 167, 285, doi: [10.3847/1538-3881/ad47c4](https://doi.org/10.3847/1538-3881/ad47c4)

Yang, A. Y., Thompson, M. A., Urquhart, J. S., & Tian, W. W. 2018, *ApJS*, 235, 3, doi: [10.3847/1538-4365/aaa297](https://doi.org/10.3847/1538-4365/aaa297)

Yang, A. Y., Urquhart, J. S., Wyrowski, F., et al. 2022, *A&A*, 658, A160, doi: [10.1051/0004-6361/202142039](https://doi.org/10.1051/0004-6361/202142039)

Yang, D., Liu, H.-L., Liu, T., et al. 2025, *ApJS*, 280, 33, doi: [10.3847/1538-4365/adf847](https://doi.org/10.3847/1538-4365/adf847)

## APPENDIX

## A. LIST OF DETECTED MOLECULAR LINES ALONG THE JET

**Table A1.** Identified Molecular Transitions in the 1.3 mm and 3 mm Bands

Species	Rest Freq. (MHz)	Quantum No.	$E_u/k$ (K)	$\log A_{ij}$ (s <sup>-1</sup> )
CO	230538.0	2–1	16.60	−6.1605
<sup>13</sup> CO	220398.7	2–1	15.87	−6.2165
C <sup>18</sup> O	219560.4	2–1	15.81	−6.2210
SiO	86847.0	2–1	6.25	−4.5335
SiO	217104.9	5–4	31.26	−3.2843
CS	97981.0	2–1	7.05	−4.7763
<sup>13</sup> CS	231220.6	5–4	22.19	−3.6008
SO	99299.9	3 <sub>2</sub> –2 <sub>1</sub>	9.23	−4.9488
SO	100029.6	4 <sub>5</sub> –4 <sub>4</sub>	38.57	−5.96577
SO	219949.4	6 <sub>5</sub> –5 <sub>4</sub>	34.98	−3.8745
OCS	231060.9	19–18	110.9	−4.4463
CCH	87316.9	1–0	4.19	−5.8161
HCN	88631.6	1–0	4.25	−4.6171
H <sup>13</sup> CN	86339.9	1–0	4.14	−4.6526
DCN	217238.5	3–2	20.85	−3.3396
HCO <sup>+</sup>	89188.5	1–0	4.28	−4.3781
H <sup>13</sup> CO <sup>+</sup>	86754.3	1–0	4.16	−4.1635
HC <sub>3</sub> N	100076.4	11–10	28.82	−4.1114
HC <sub>3</sub> N	218324.7	24–23	130.98	−3.0830
HNCO	219798.3	10 <sub>0,10</sub> –9 <sub>0,9</sub>	58.02	−3.8329
H <sub>2</sub> CO	101333.0	6 <sub>1,5</sub> –6 <sub>1,6</sub>	87.56	−5.8038
H <sub>2</sub> CO	218222.2	3 <sub>0,3</sub> –2 <sub>0,2</sub>	20.96	−3.5501
H <sub>2</sub> CO	218475.6	3 <sub>2,2</sub> –2 <sub>2,1</sub>	68.09	−3.8037
H <sub>2</sub> CO	218760.1	3 <sub>2,1</sub> –2 <sub>2,0</sub>	68.11	−3.8021
H <sub>2</sub> <sup>13</sup> CO	219908.5	3 <sub>1,2</sub> –2 <sub>1,1</sub>	32.94	−3.5911
CH <sub>3</sub> OH (A)	97582.8	2 <sub>–1,1</sub> –1 <sub>–1,0</sub>	21.56	−5.5807
CH <sub>3</sub> OH (E)	216945.5	5 <sub>–1,4</sub> –4 <sub>–2,3</sub>	55.87	−4.9159
CH <sub>3</sub> OH (E)	218440.1	4 <sub>–2,3</sub> –3 <sub>–1,2</sub>	45.46	−4.3292
CH <sub>3</sub> OH (E)	220078.6	8 <sub>–0,8</sub> –7 <sub>–1,6</sub>	96.61	−4.5993
CH <sub>3</sub> CN	220730.3	12 <sub>2</sub> –11 <sub>2</sub>	97.44	−3.0465
CH <sub>3</sub> CN	220743.0	12 <sub>1</sub> –11 <sub>1</sub>	76.01	−3.0372
CH <sub>3</sub> CN	220747.3	12 <sub>0</sub> –11 <sub>0</sub>	68.67	−3.0342
CH <sub>3</sub> CHO (E)	98863.3	5 <sub>1,4</sub> –4 <sub>1,3</sub>	16.59	−4.5082
CH <sub>3</sub> CHO (A)	98900.9	5 <sub>1,4</sub> –4 <sub>1,3</sub>	16.51	−4.5077
CH <sub>3</sub> OCHO (A+E)	216966	20–19	111.5	−3.815

NOTE— CH<sub>3</sub>OCHO and CH<sub>3</sub>CN are marginally detected.

Table A1 summarizes all molecular transitions detected at the bright knots of the outflow. The corresponding spectra are shown in Fig. A1 and A2, overlaid with cumulative integrated intensity curves.

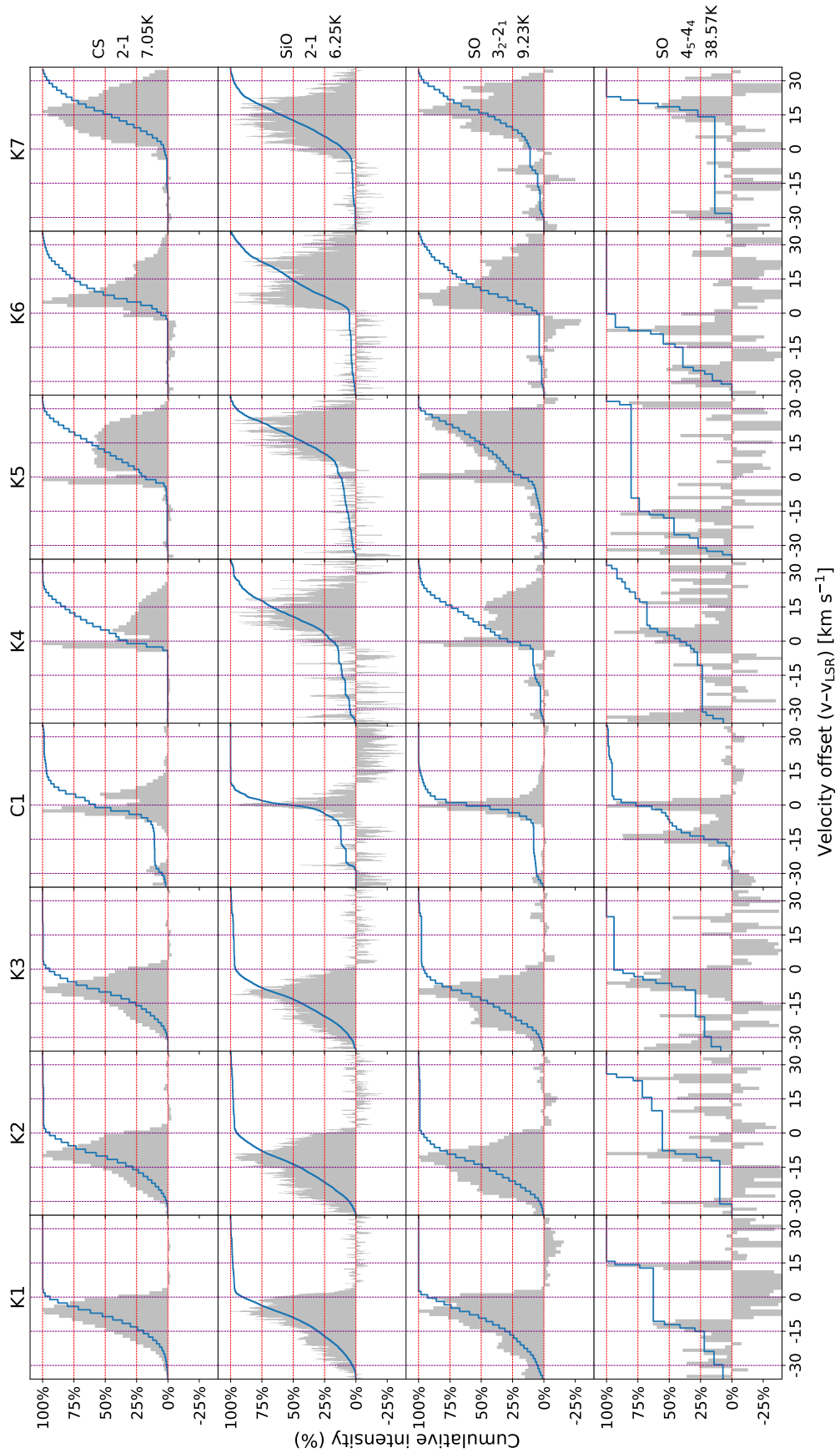


Figure A1. (a) Identified molecular transitions in the 3-mm Band.

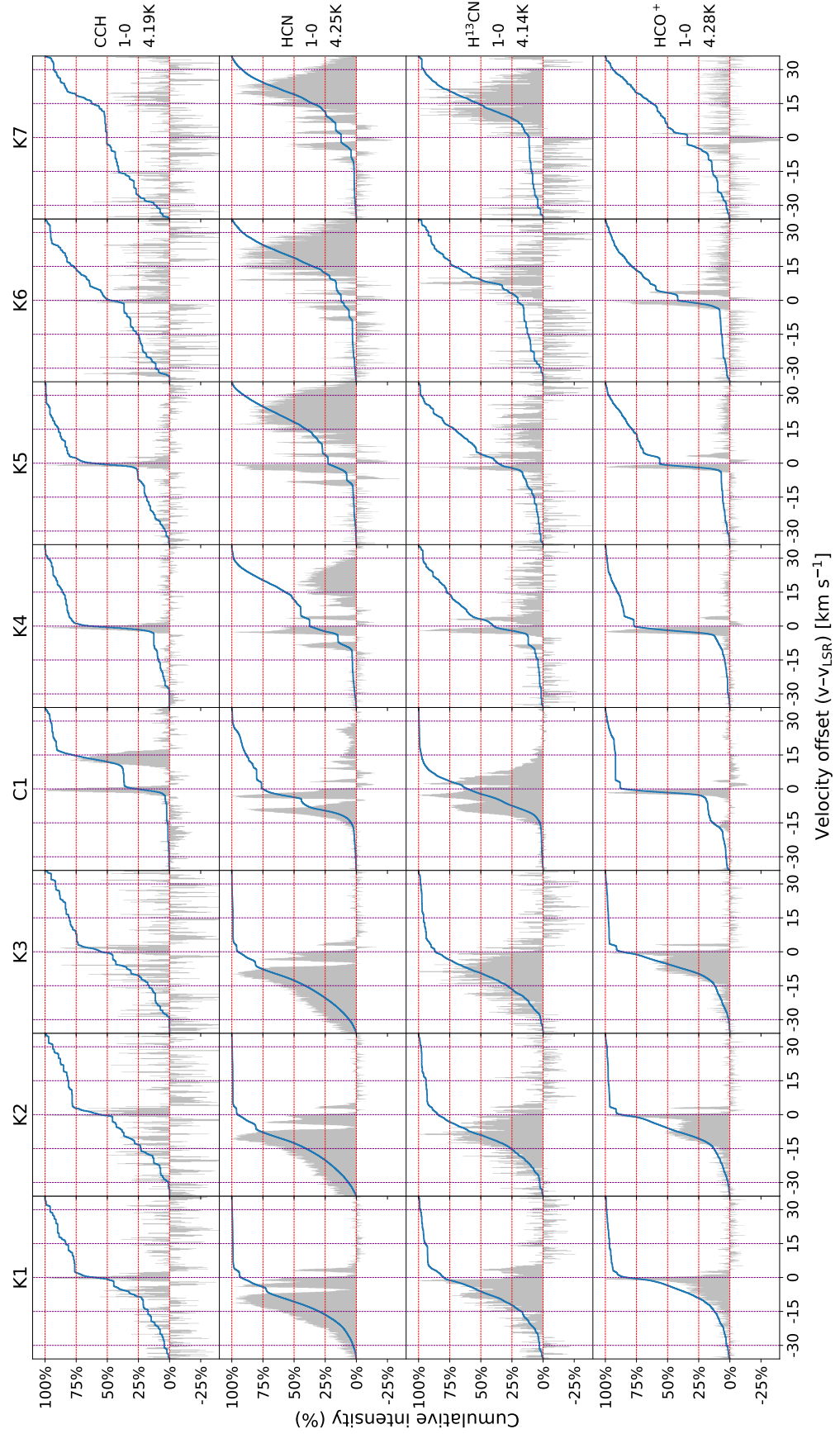


Figure A1. (b) Continued.

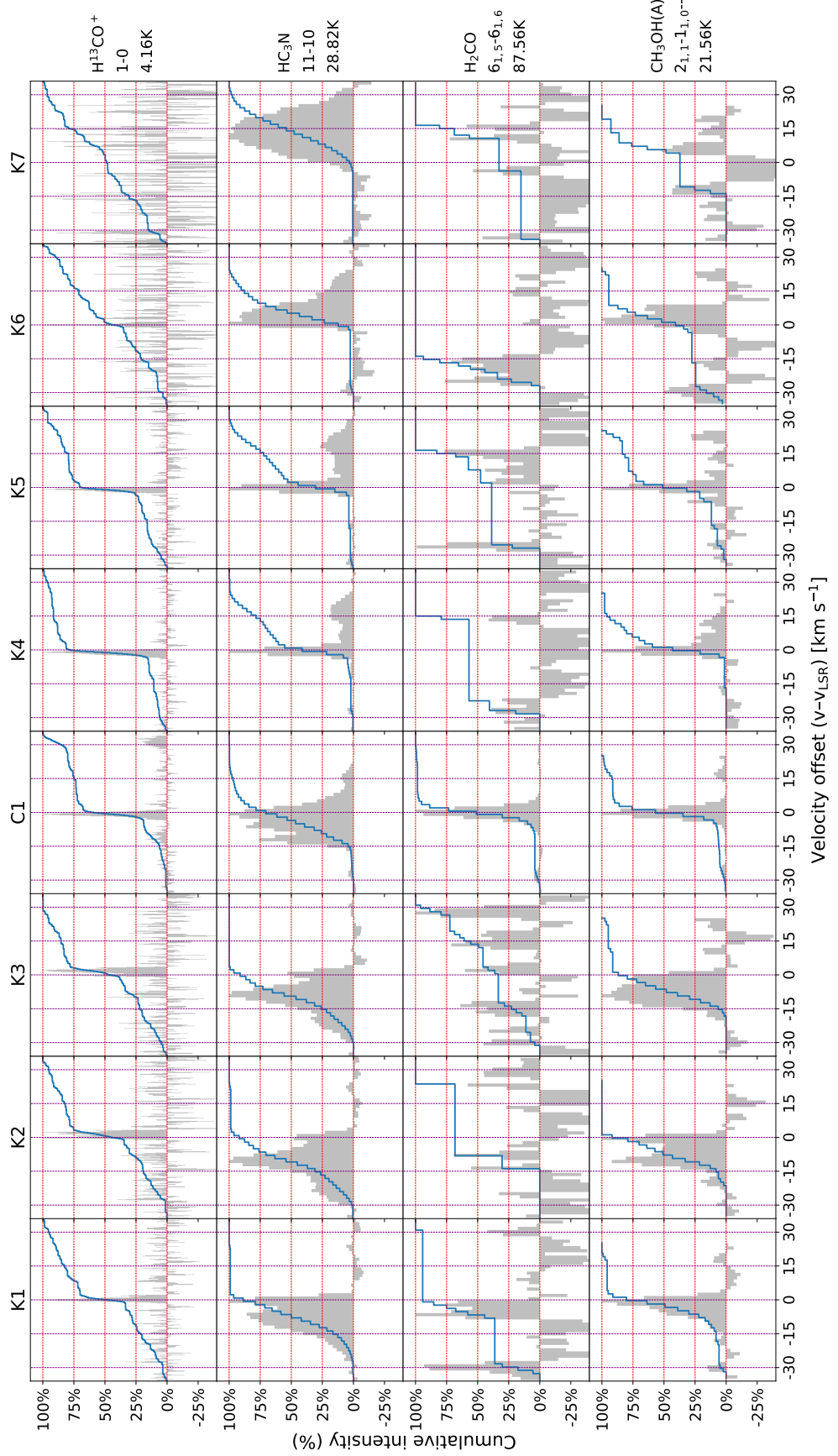


Figure A1. (c) Continued.

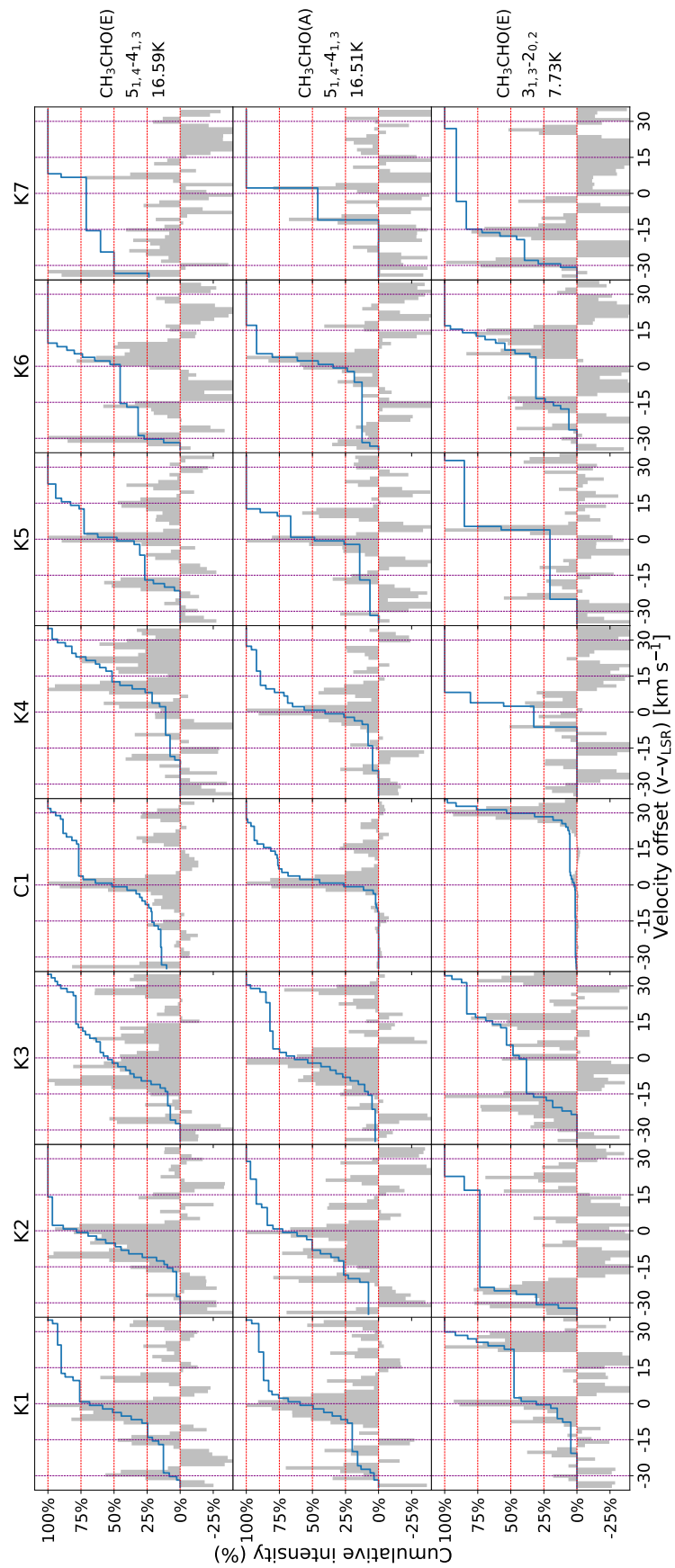
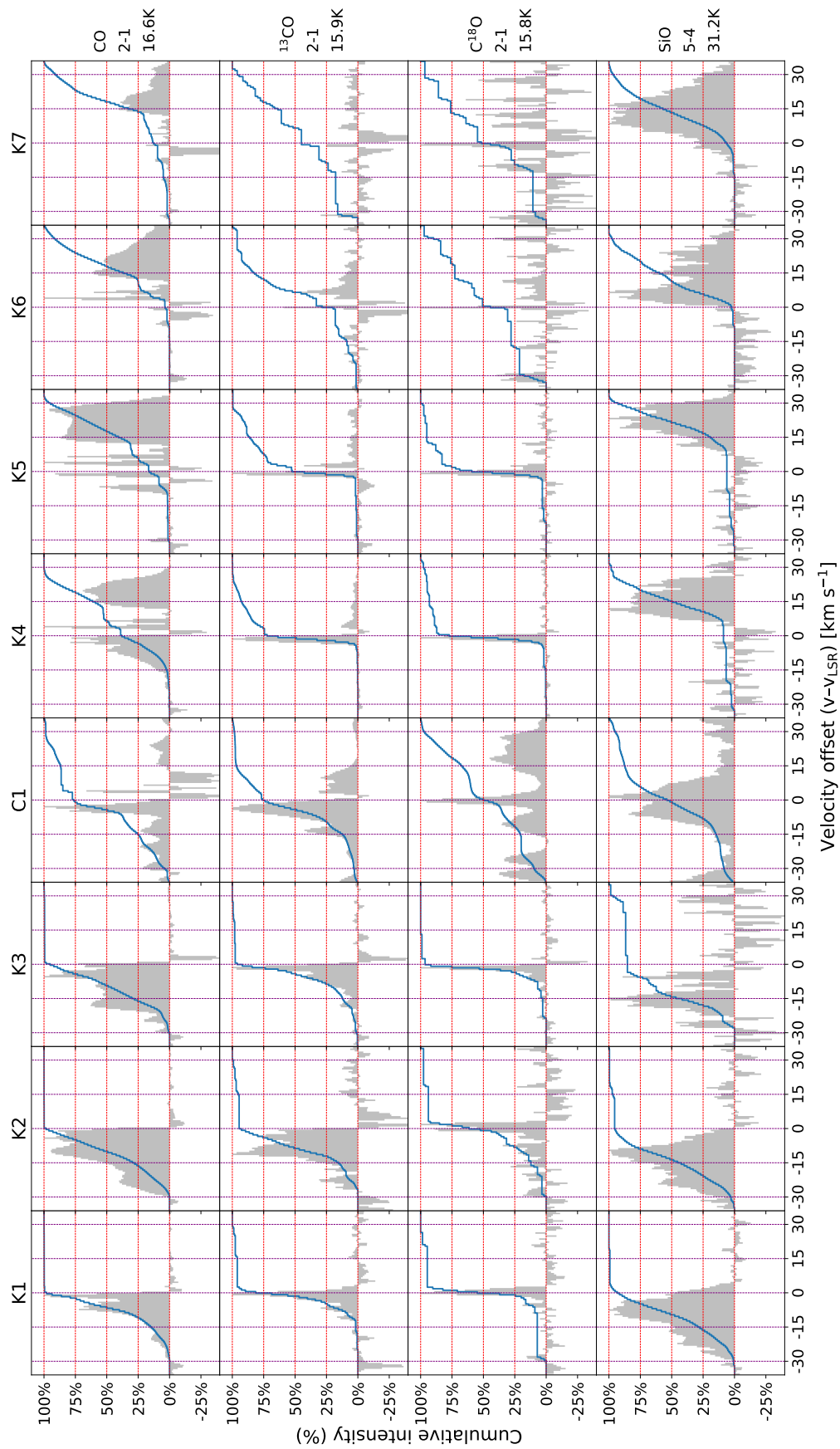
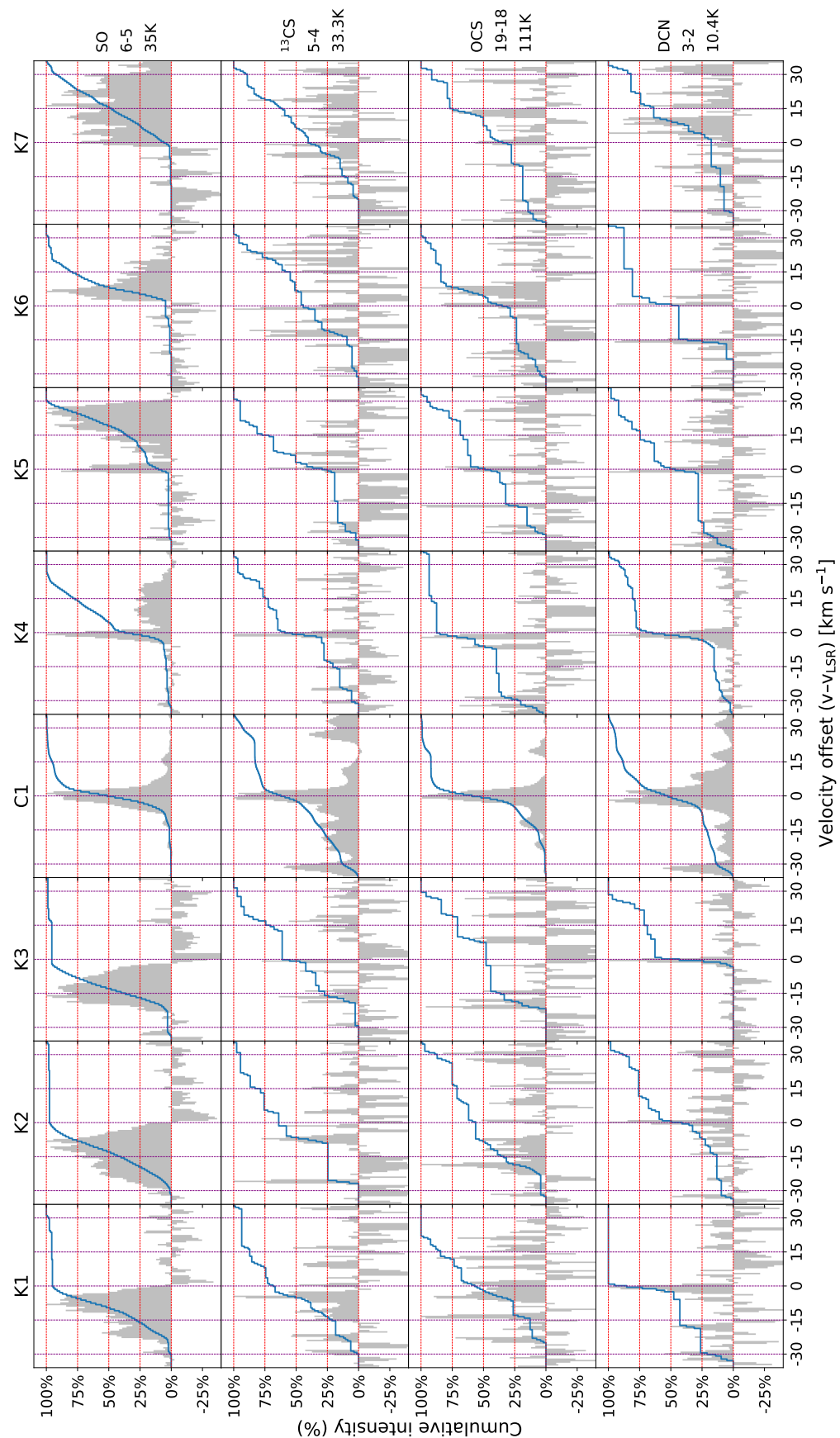


Figure A1. (d) Continued.



**Figure A2.** (a) Identified molecular transitions in the 1.3-mm Band.



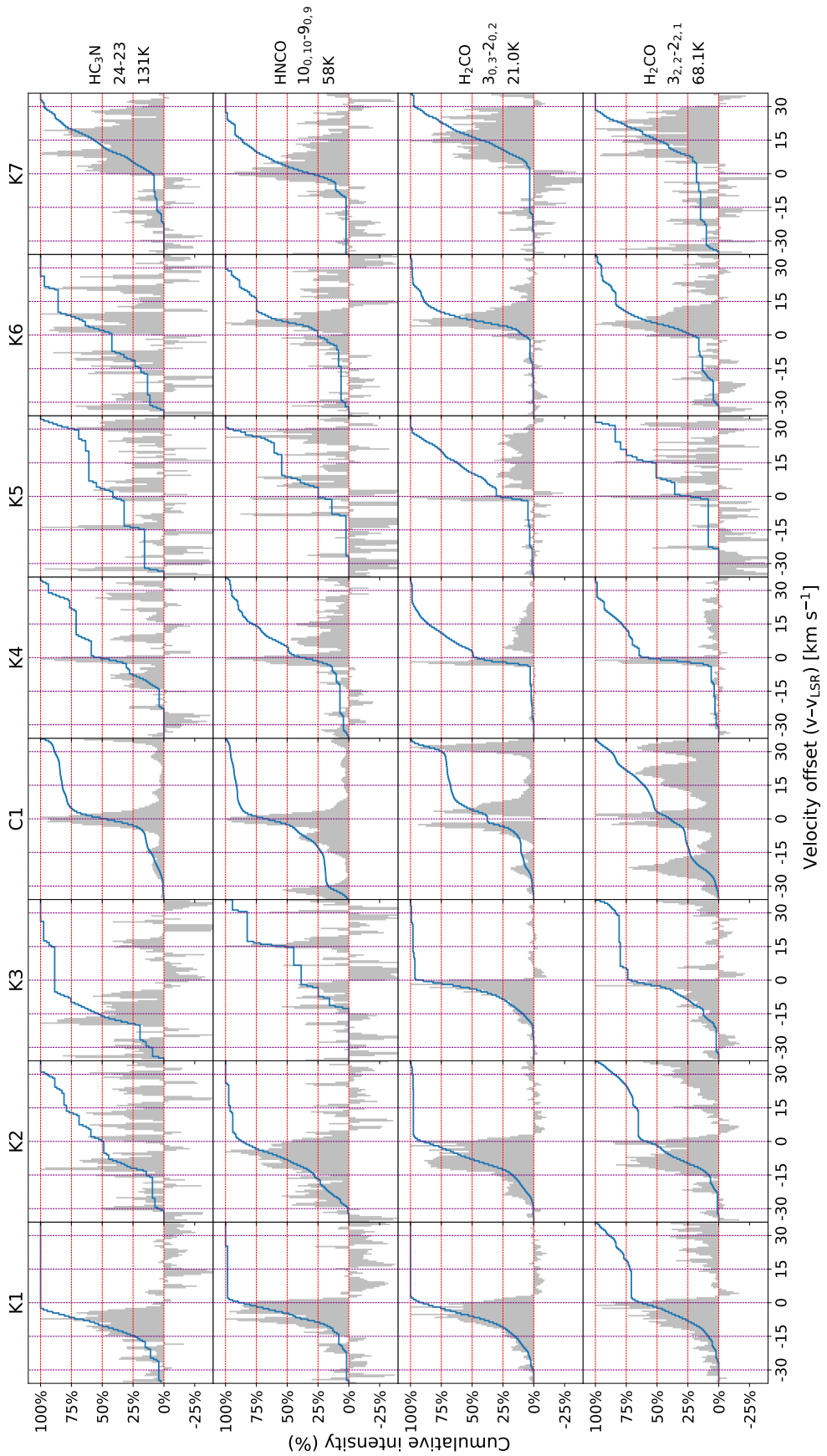


Figure A2c. (c) Continued.

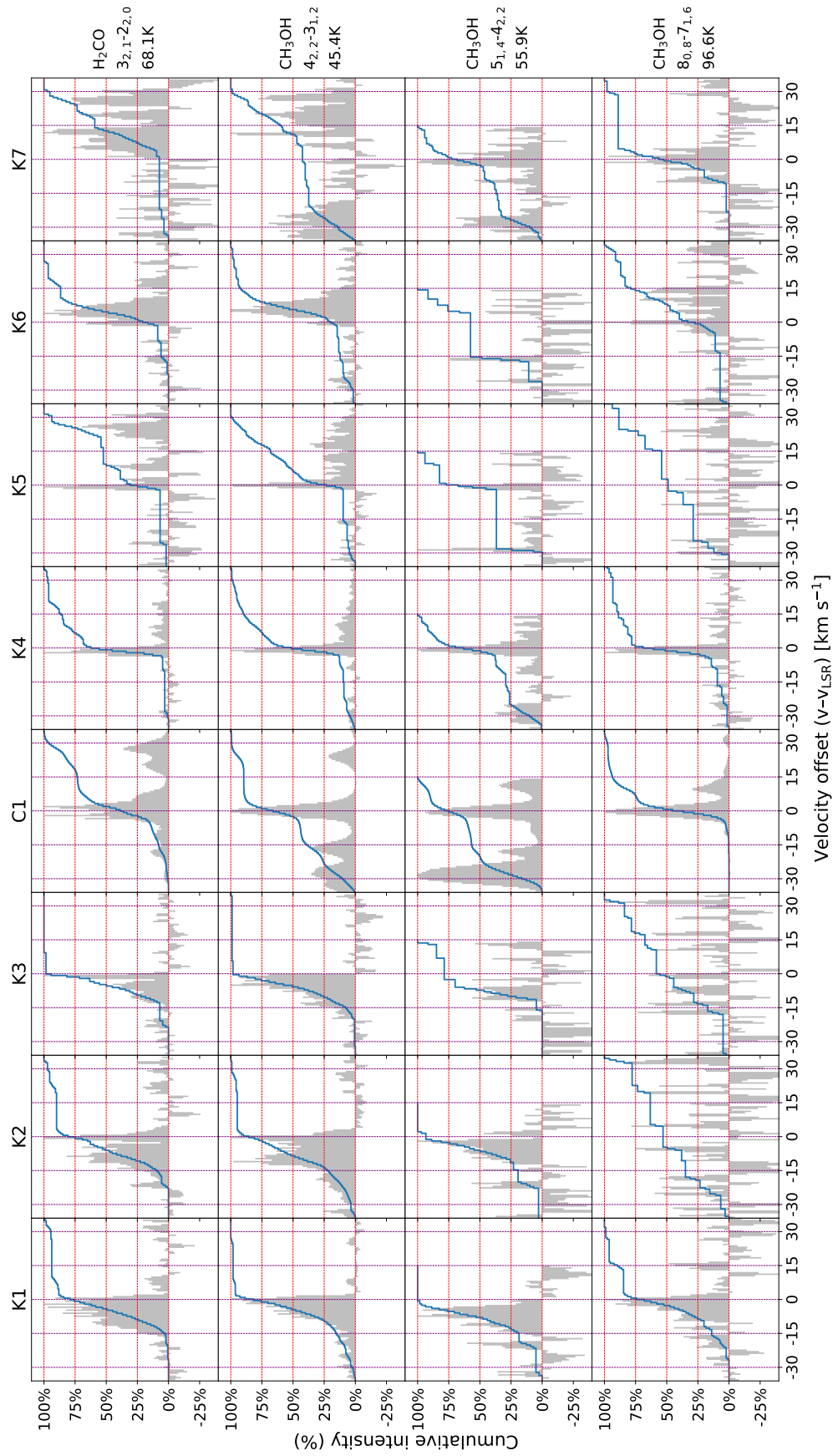


Figure A2. (d) Continued.

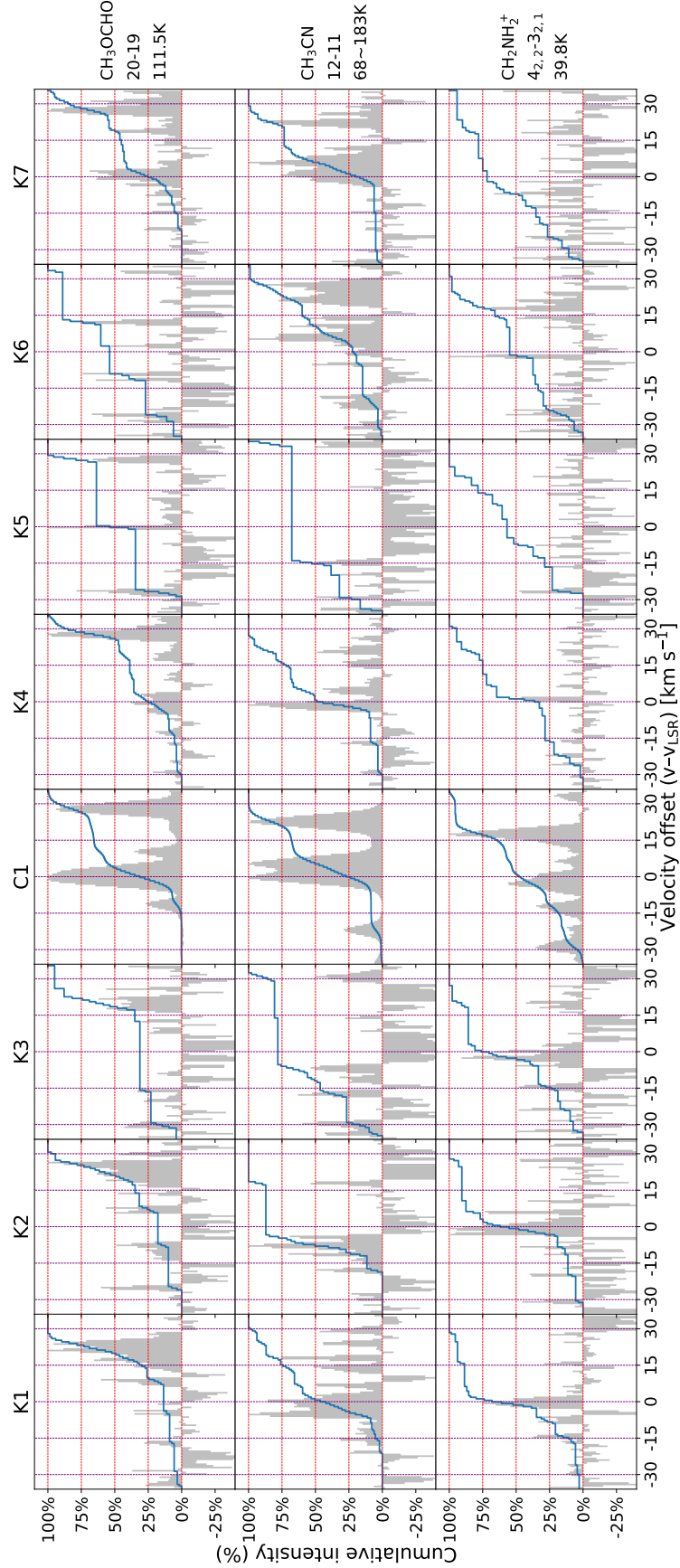


Figure A2. (e) Continued. The U line in Fig. 4 and Fig. 5 here is marked as  $\text{CH}_2\text{NH}_2^{+*}$ .

## B. SUPPLEMENTARY POSITION-VELOCITY ANALYSIS

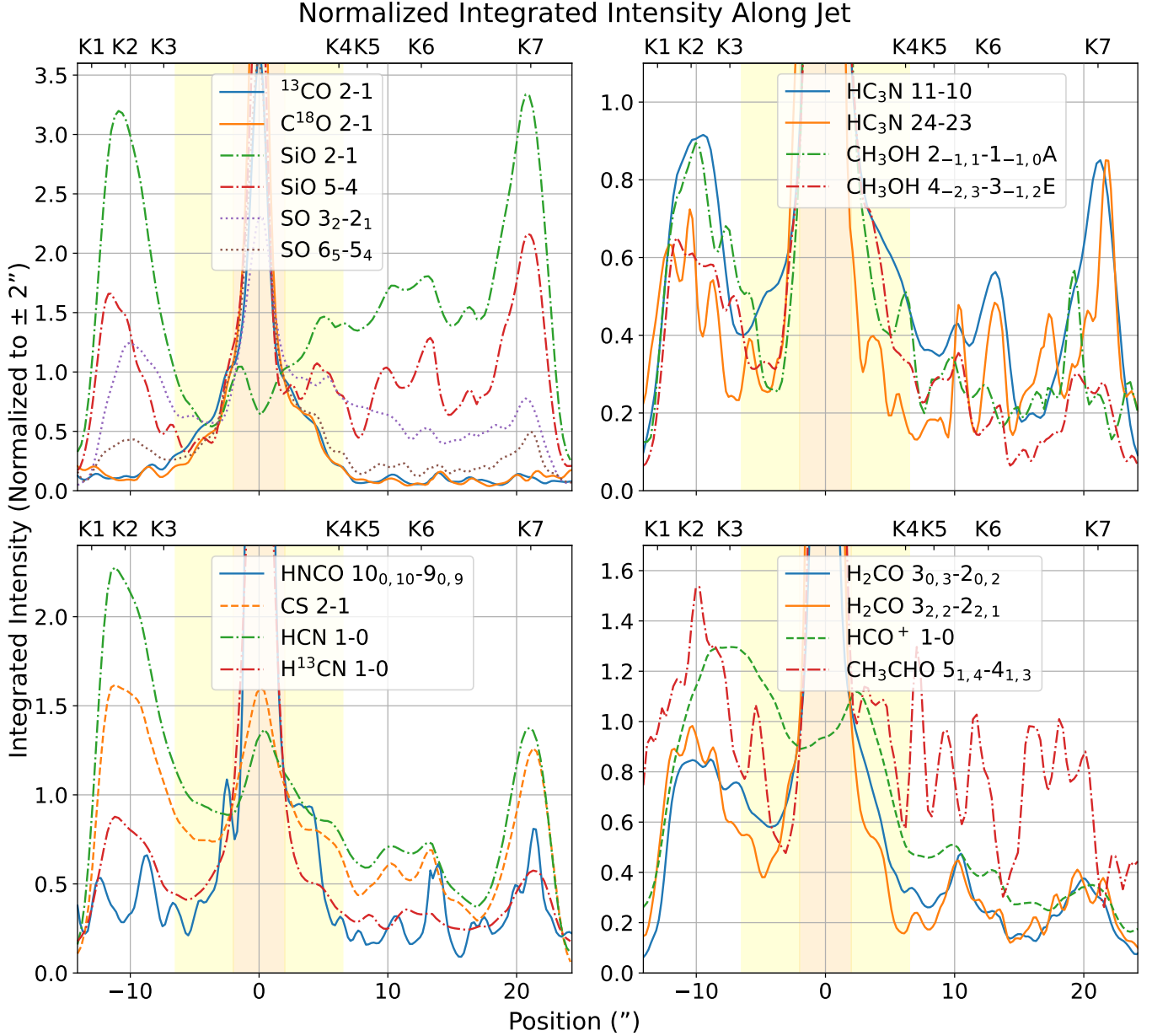
Fig. B1 presents the integrated intensity along the outflow axis defined in Fig. 1(a), with a slit width of  $1''$  and velocity range from  $-36$  to  $+36$  km s $^{-1}$ . Based on the spatial distributions of the continuum, CCH, C $^{18}$ O and other molecules (see Fig. 1(b) and Fig. 2), we consider the inner  $2''$  to be dominated by hot-core emission. To minimize this contamination, all values are divided by the reference intensity at  $2''$  from the core; regions beyond  $2''$  are referred to as the “pure” outflow in the following discussion. The integrated intensities of  $^{13}$ CO and C $^{18}$ O decrease monotonically with distance, whereas other molecules show oscillatory enhancements.

Because the outflow expands with distance, absolute integrated intensities are not direct tracers of abundance variations. Fig. B2 therefore shows the ratios of each molecule to the local  $^{13}$ CO intensity, normalized at each position, to reveal abundance gradients. Compared with Fig. B1, the relative abundances display mirror symmetry with respect to the hot core, particularly within  $\pm 14''$ , consistent with the integrated maps (Fig. 2) and PVDs (Fig. 3). The middle outflow ( $2''$ – $6.5''$ ) exhibits systematically lower abundances, highlighted with a pale yellow background. Fig. B3 further zooms into shock–weak regions: after re-normalization at  $2''$ , the vertical axis shows the abundance relative to the  $2''$  value. The mean and standard deviation of “abundance factors relative to  $^{13}$ CO” are adopted to assess significance, as annotated in the figure. SO  $6_5$ – $5_4$ , HC<sub>3</sub>N, both H<sub>2</sub>CO transitions, CH<sub>3</sub>OH-E, H $^{13}$ CN, and HNCO remain nearly constant, suggesting weak shock sensitivity; by contrast, SiO, SO  $3_2$ – $2_2$ , CS, HCO $^+$ , HCN, CH<sub>3</sub>OH-A, and CH<sub>3</sub>CHO show various levels of enhancement, pointing to distinct formation pathways.

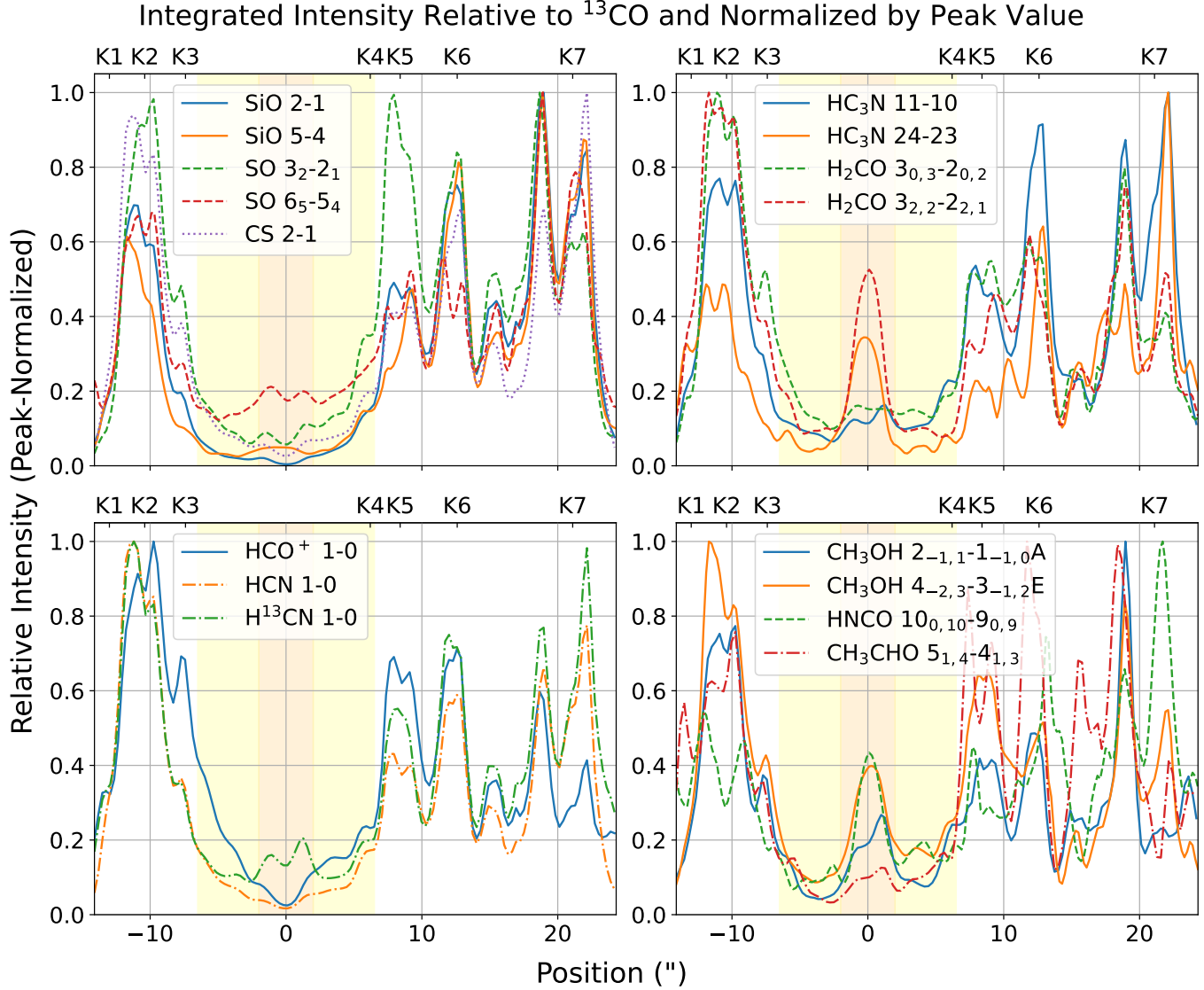
Fig. B4 shows the variation rate of SiO  $5_4$ – $4_3$  intensity compared with the kinetic temperature  $T_{\text{kin}}$  derived from H<sub>2</sub>CO 3–2 transitions. The kinetic temperature is calculated using the non-LTE radiative transfer code RADEX (F. F. S. van der Tak et al. 2007). We assume the volume density  $10^5$ – $10^6$  cm $^{-3}$  of the outflow, and using minimum  $\chi^2$  to optimize the line ratio between transitions of H<sub>2</sub>CO 3–2. This method has a good constrain of temperature below 300 K otherwise the temperature can be sensitive to the volume density. Bright knots correspond to high  $T_{\text{kin}}$  and steep SiO gradients, indicating that jet impacts compress and heat the outflowing shell, leading to the release of icy species into the gas phase.

Fig. B5 compares selected line profiles in the 1.3 mm and 3 mm bands. The cumulative intensity at the bottom separates systemic and non-systemic velocity components to highlight differences.

- (a) High-velocity molecules at 1.3 mm: SiO, SO, HC<sub>3</sub>N. For HC<sub>3</sub>N the S/N is low at knots K2, K3, K5, and K6, but near-Gaussian at C1.
- (b) High-velocity molecules at 3 mm: SiO, CS, SO, HCN, HC<sub>3</sub>N. Overall profiles resemble those at 1.3 mm, but the cumulative plots differ significantly: SiO and SO dominate  $|v| > 12$  km s $^{-1}$ , while CS and HC<sub>3</sub>N are weaker; H $^{13}$ CN lies in between.
- (c) Low-velocity molecules at 1.3 mm: HNCO, H<sub>2</sub>CO, CH<sub>3</sub>OH-E, CH<sub>3</sub>CN. The three adjacent CH<sub>3</sub>CN  $12_k$ – $11_k$  lines show absorption at knots K3–K5, indicating excitation temperatures lower than the outflow background. HNCO has insufficient S/N at some knots. These species are dominated by systemic velocity emission (see Fig. 2), with weaker high- and low-velocity components.
- (d) Low-velocity molecules at 3 mm: HCO $^+$ , CH<sub>3</sub>OH-A, CH<sub>3</sub>CHO. CH<sub>3</sub>OH-A ( $E_u = 21.1$  K) is more concentrated at systemic velocity compared with CH<sub>3</sub>OH-E ( $E_u = 45.5$  K), and shows stronger emission in the northern (redshifted) lobe. Whether this A/E difference reflects intrinsic nuclear-spin properties remains to be confirmed.



**Figure B1.** Integrated intensities of selected molecular lines along the jet axis of SDC335, plotted as a function of projected distance from the central hot core (C1). All intensities are normalized to their values at  $\pm 2''$  to highlight relative enhancements or suppressions along the flow. Positive offsets correspond to the northern (red-shifted) lobe, and negative offsets to the southern (blue-shifted) lobe.



**Figure B2.** Relative abundance proxies of selected molecules along the jet axis, computed as the ratio of their integrated intensities to that of  $^{13}\text{CO}$  at each position. Each line is normalized to its own maximum value across the spatial extent to emphasize the distribution pattern rather than absolute abundance contrast. This highlights molecule-specific spatial differentiation along the outflow.

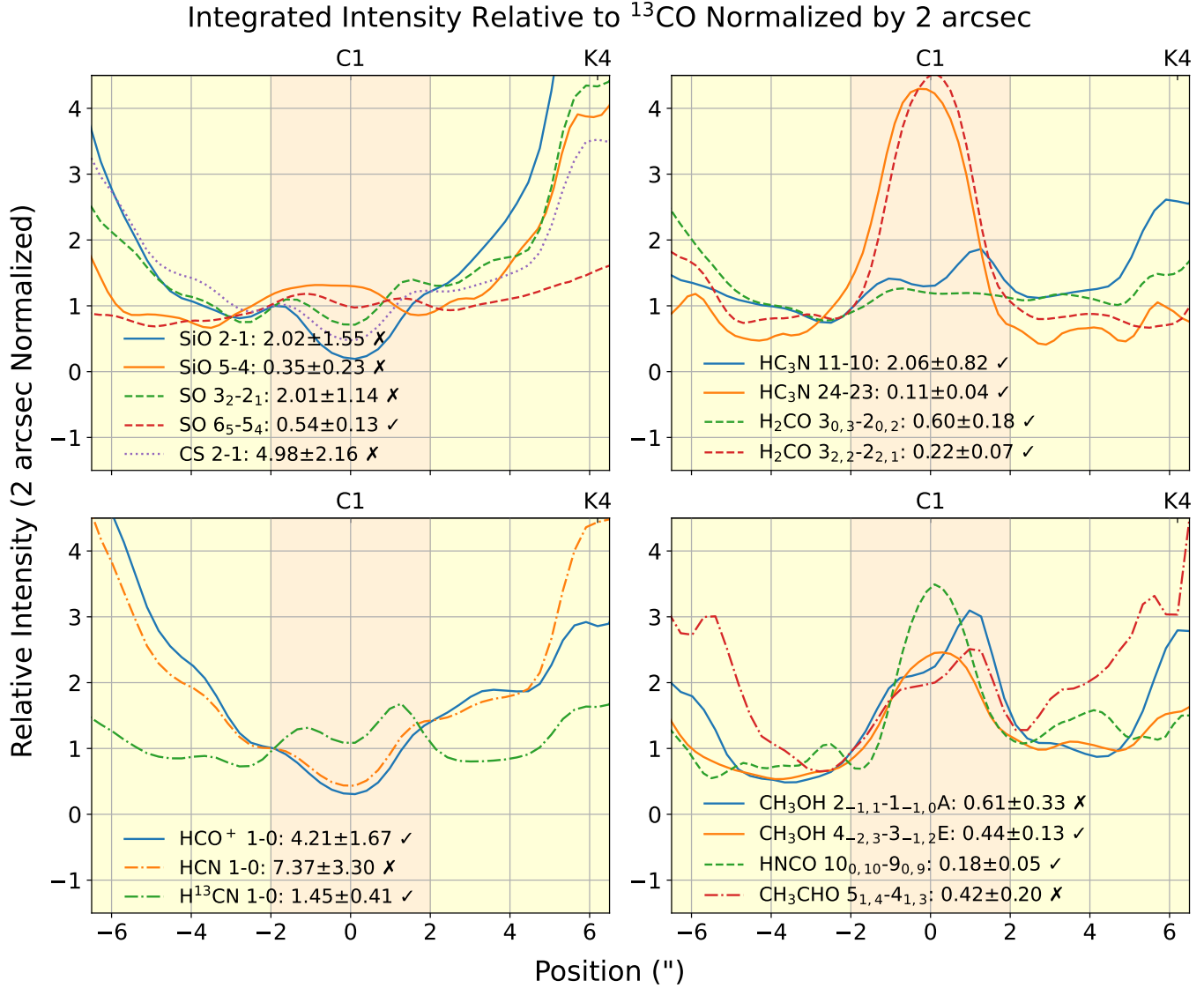


**Figure B3.** An enlarged view of the weak-shock region (light yellow background) in Figure B2, showing that some transitions, such as  $\text{H}_2\text{CO}$   $3_{0,3}-2_{0,2}$  and  $\text{SO}$   $6_5-5_4$ , exhibit relatively little variation in intensity within this range, whereas other transitions show significant intensity changes.

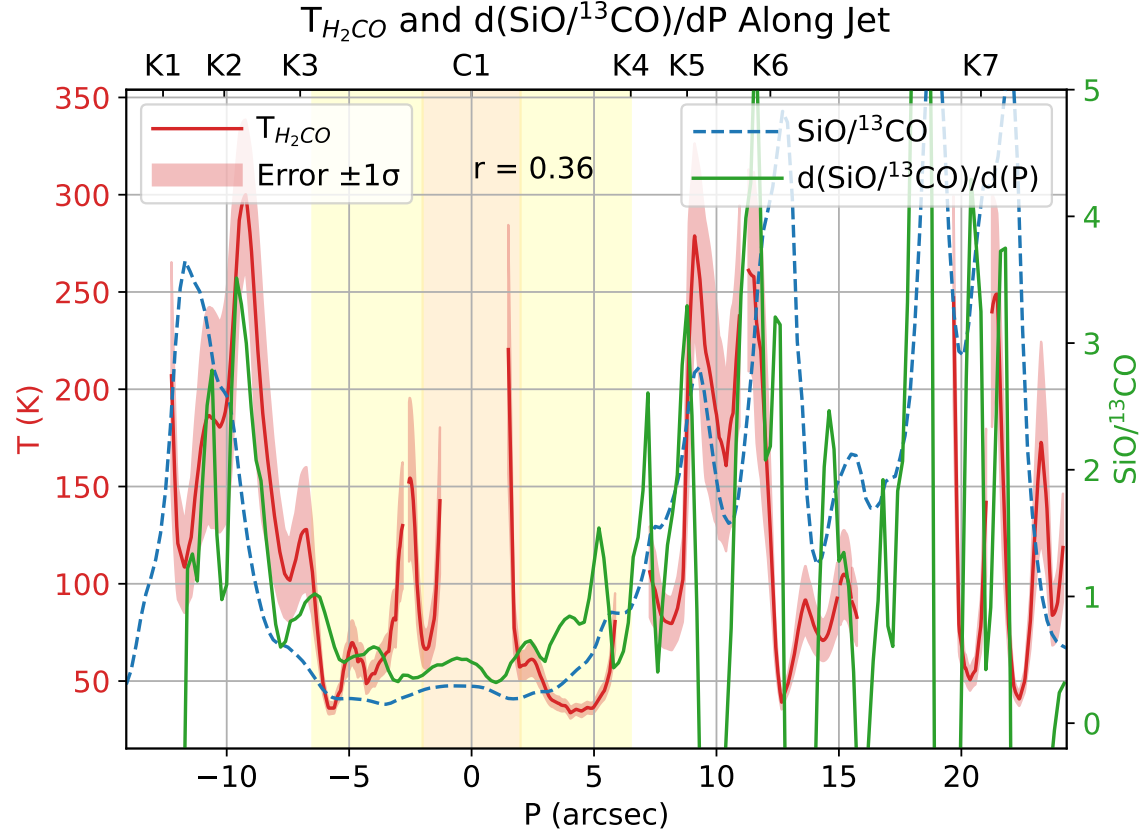


**Figure B4.** Comparison between the rotational temperature ( $T_{\text{rot}}$ ) derived from  $\text{H}_2\text{CO}$  and the spatial derivative of the  $\text{SiO}$ -to- $^{13}\text{CO}$  integrated intensity ratio along the outflow axis of SDC335. The horizontal axis represents the projected distance from the central hot core, while the two vertical axes show  $T_{\text{rot}}$  (in K, left axis) and  $d(\text{SiO}/^{13}\text{CO})/dP$  where  $P$  is position (right axis). The central light orange background indicates the extent of the hot core and its warm envelope, while the flanking light yellow regions mark areas in the outflow where some molecules do not show significant weakening relative to  $^{13}\text{CO}$ . Regions with elevated  $\text{SiO}$  5–4 gradients coincide with local temperature peaks, indicating strong shock heating and enhanced molecular desorption.

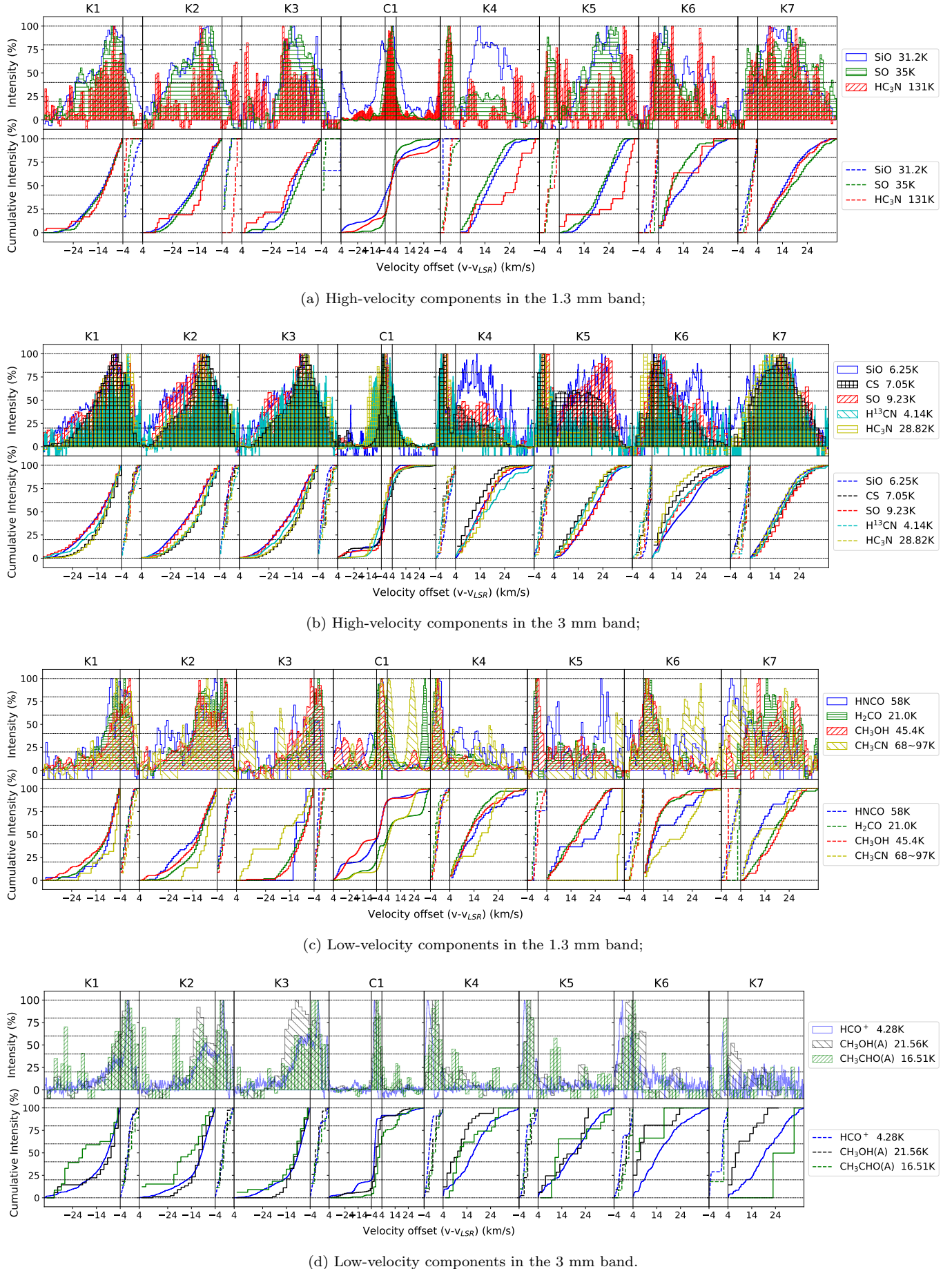


**Figure B5.** The cumulative curves quantify the total line flux for each source, aiding comparison between knots and the central core.

### C. CHANNEL MAPS

We also produced channel maps of CO,  $^{13}\text{CO}$ , SiO, SO, H<sub>2</sub>CO, and CH<sub>3</sub>OH using the combined ACA+TM1+TM2 data with angular resolution of  $0.34''$ . To suppress random noise in single channels, we integrated over  $\pm 1.3 \text{ km s}^{-1}$  centered on each velocity (this is also why these data were not used for quantitative analysis). The maps show that the high-velocity jet is located along the outflow axis, while the low-velocity component forms cavity-like structures. The maximum velocities reach  $\pm 36 \text{ km s}^{-1}$  for SiO and  $\pm 33 \text{ km s}^{-1}$  for SO. Components with  $|v| > 12 \text{ km s}^{-1}$  are concentrated near the axis, whereas slower components attach to the cavity walls. H<sub>2</sub>CO and CH<sub>3</sub>OH follow similar trends, with maximum velocities of  $\pm 27 \text{ km s}^{-1}$  and  $\pm 24 \text{ km s}^{-1}$ , respectively. Several smaller-scale jets in other directions are also discernible in these maps.

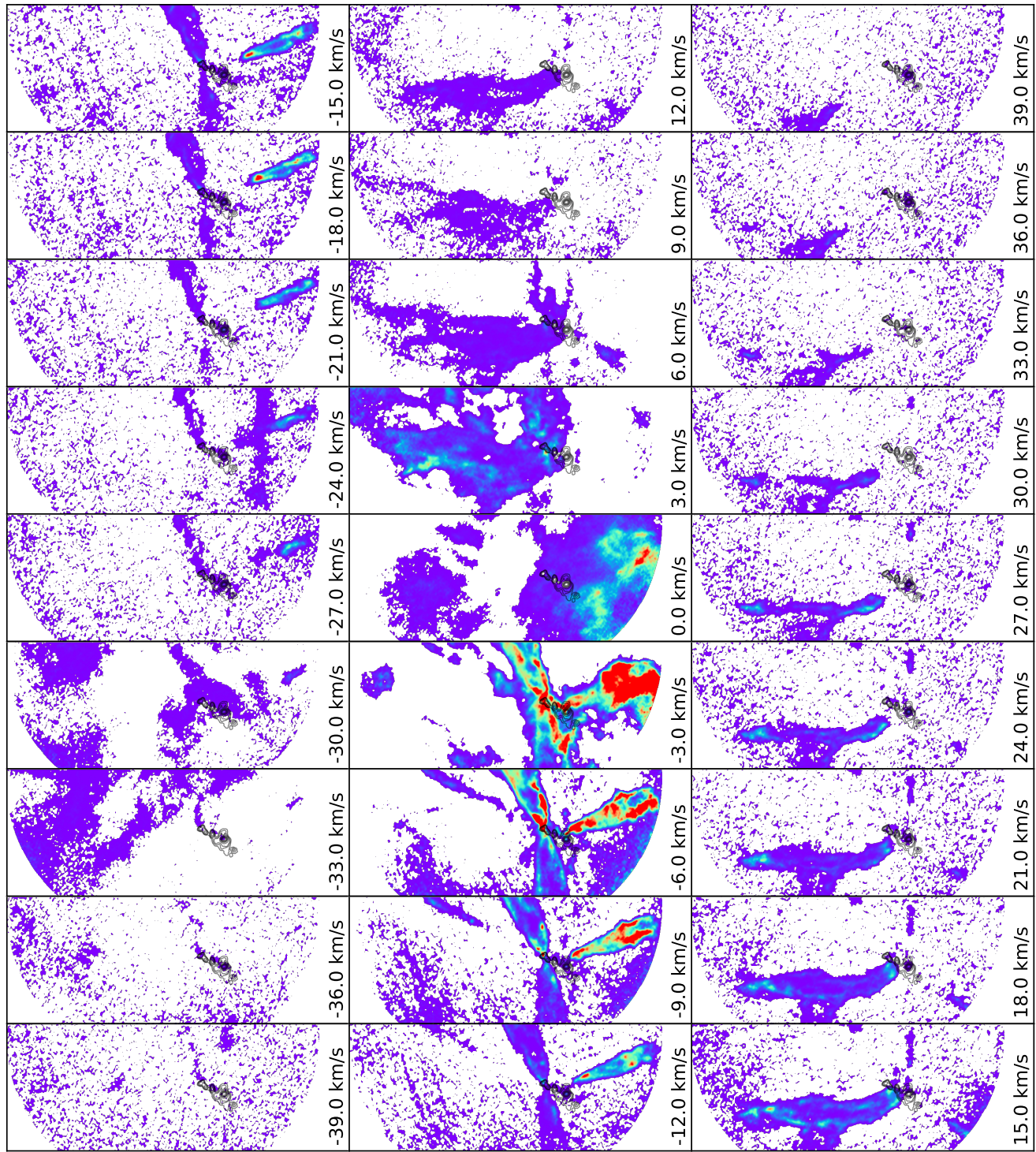


Figure C1. CO 2-1 channel map.

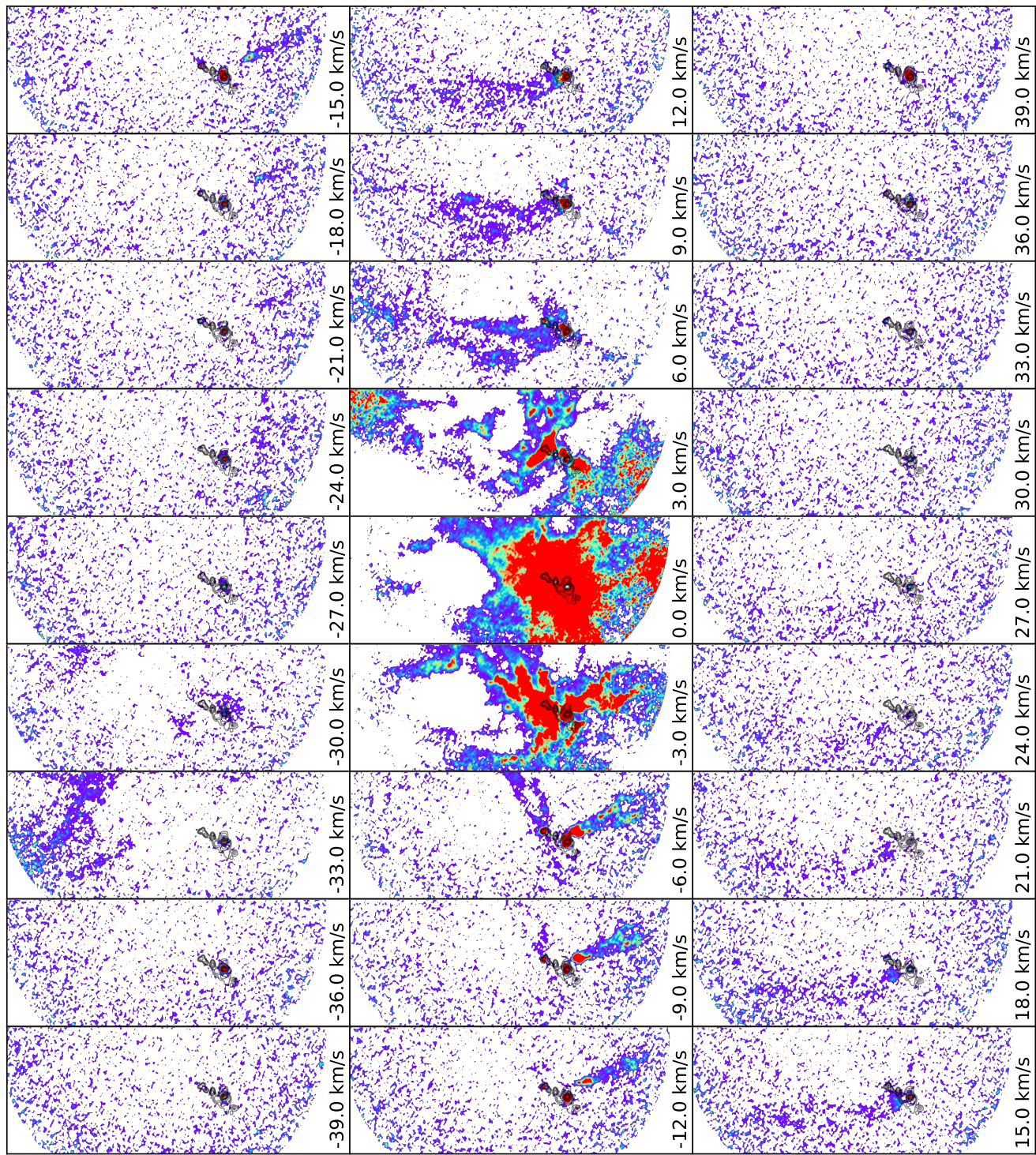


Figure C2.  $^{13}\text{CO}$  2-1 channel map.

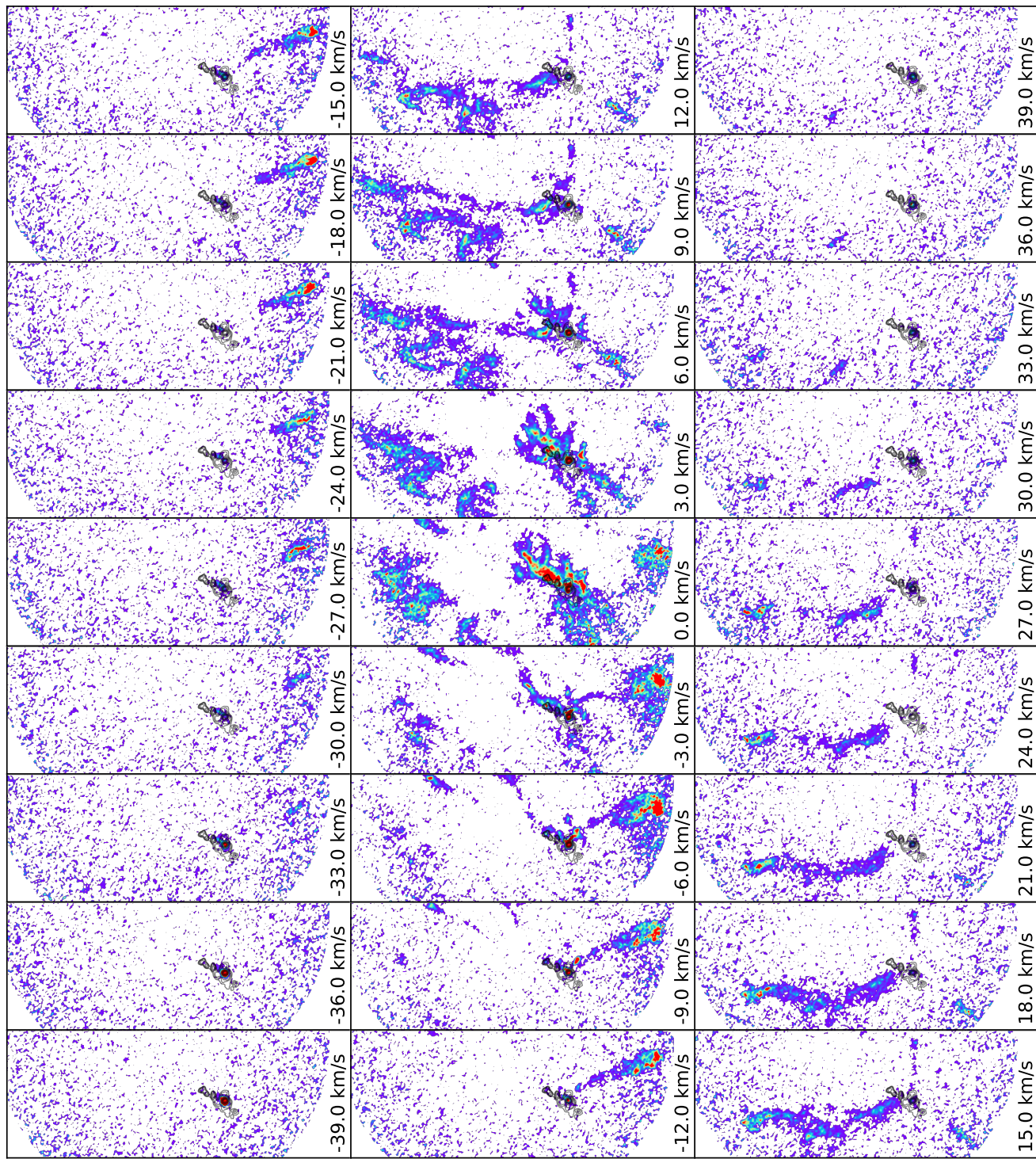


Figure C3. SiO 5-4 channel map.

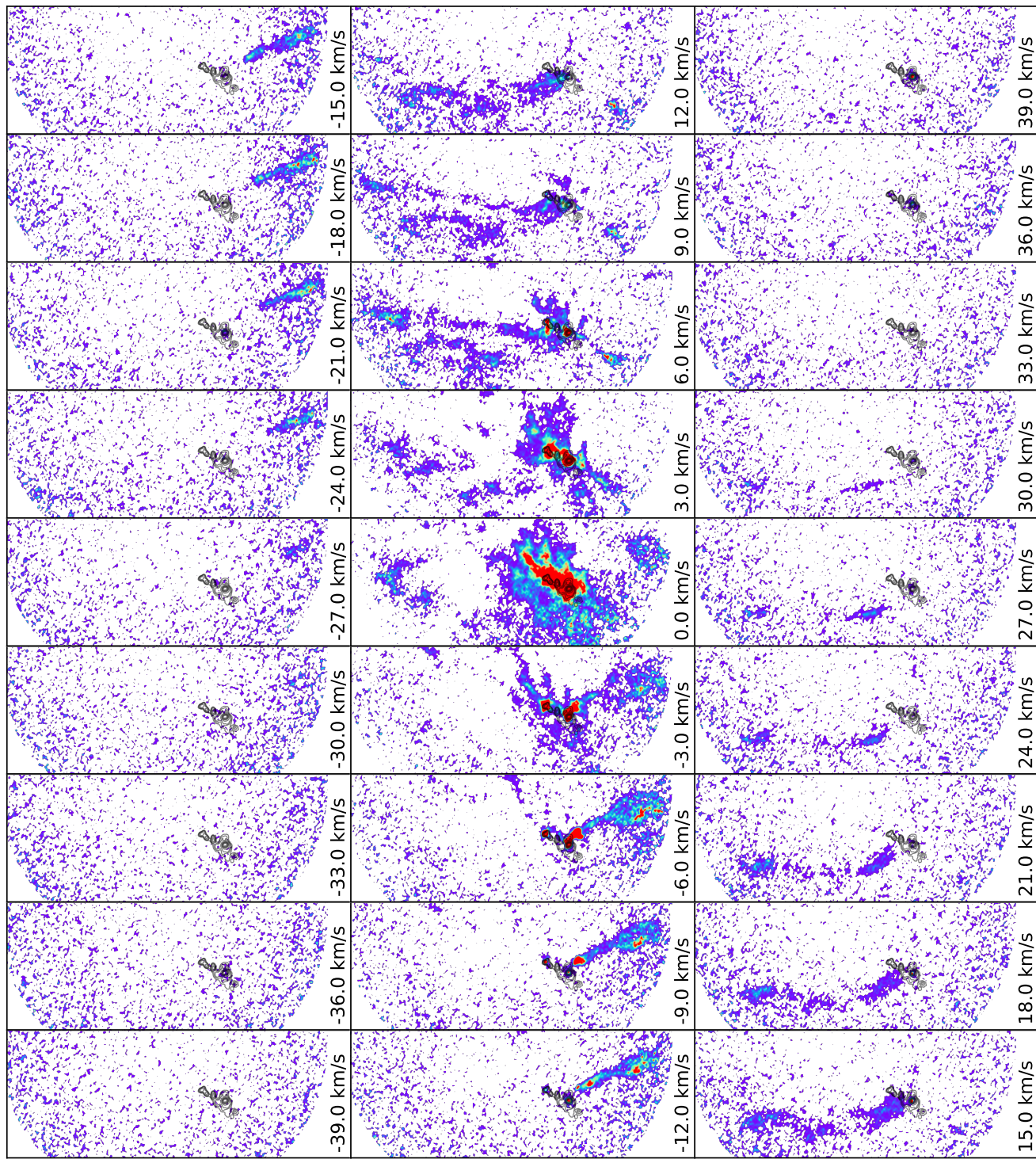
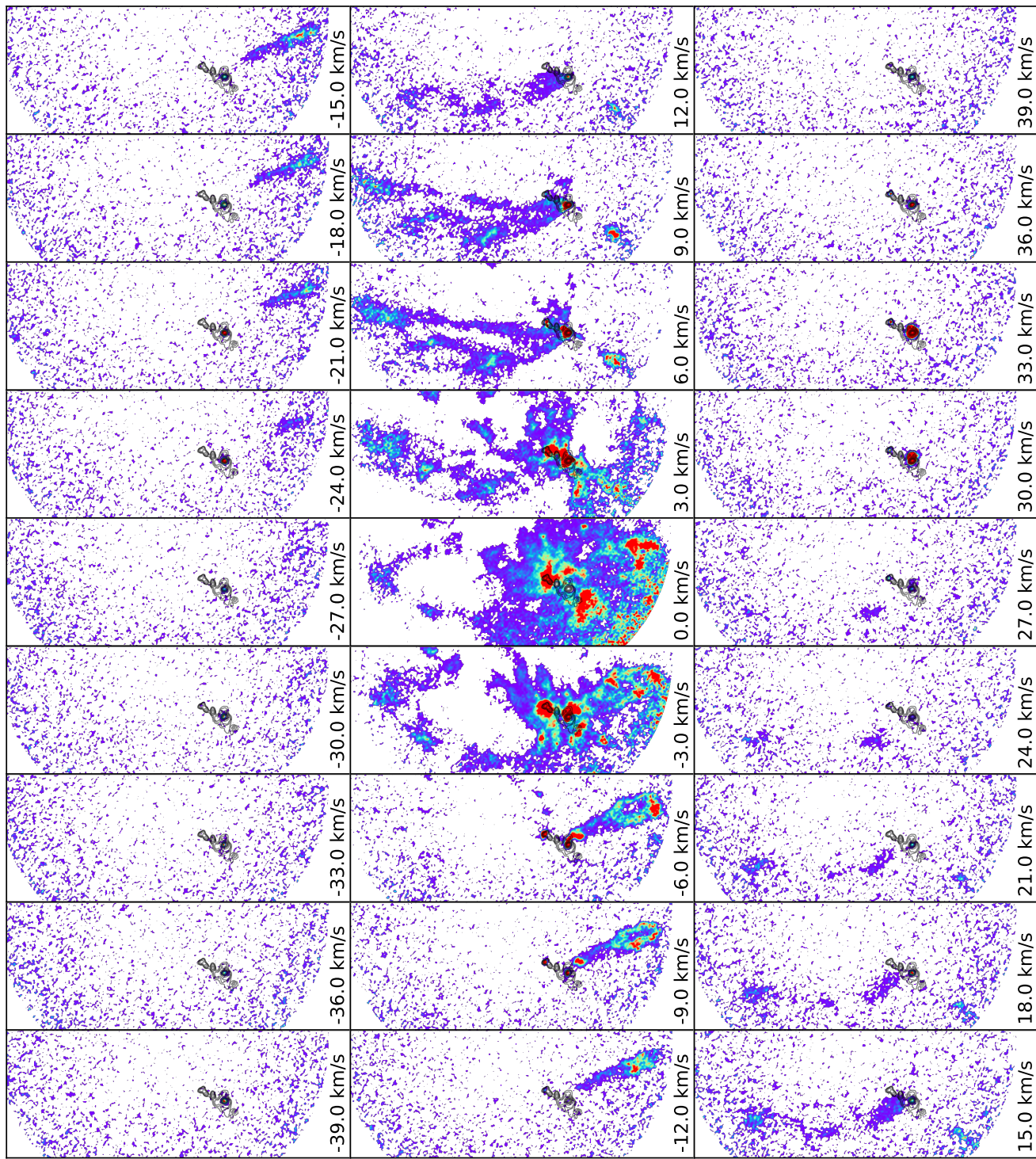


Figure C4. SO  $6_5-5_4$  channel map.

Figure C5.  $\text{H}_2\text{CO}$   $30,3-20,2$  channel map.

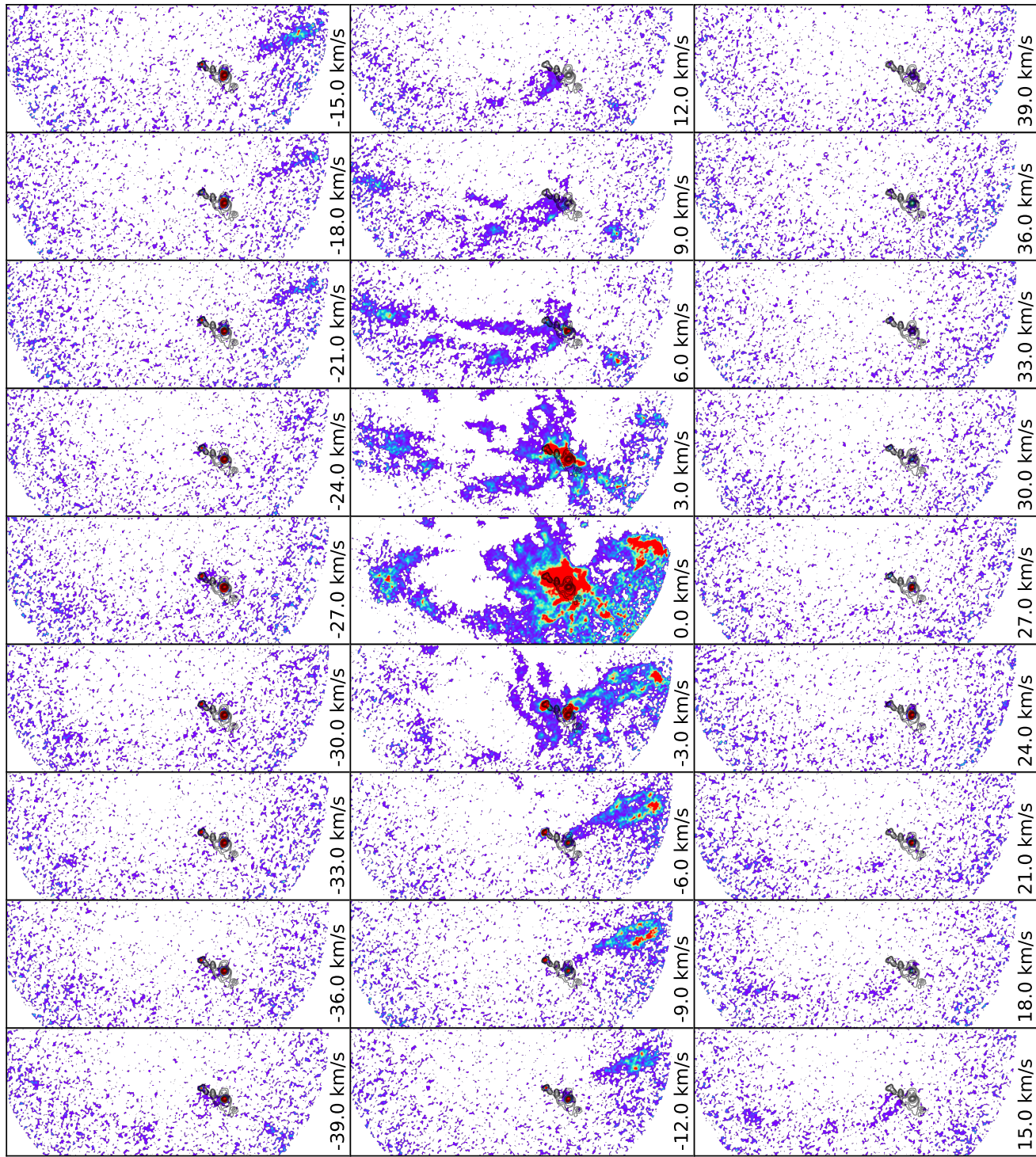


Figure C6.  $\text{CH}_3\text{OH}$   $4-2,3 - 3-1,2$  channel map.